CHALMERS

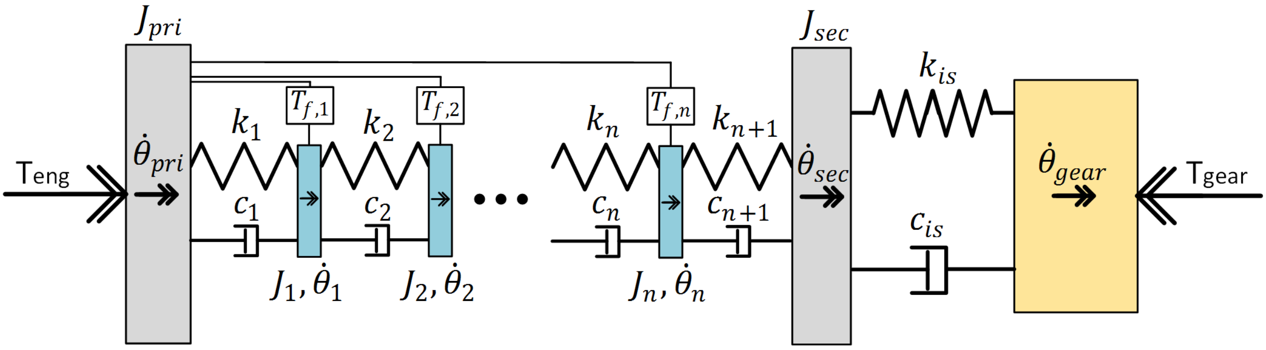

Simulation Models of Dual Mass Flywheels

Master's thesis in Applied Mechanics

DANIEL JOHANSSON
KIM KARLSSON

Department of Applied Mechanics
CHALMERS UNIVERSITY OF TECHNOLOGY
Göteborg, Sweden 2017

MASTER'S THESIS IN APPLIED MECHANICS

Simulation Models of Dual Mass Flywheels

DANIEL JOHANSSON
KIM KARLSSON

Department of Applied Mechanics

Division of Dynamics

CHALMERS UNIVERSITY OF TECHNOLOGY

Göteborg, Sweden 2017

Simulation Models of Dual Mass Flywheels
DANIEL JOHANSSON
KIM KARLSSON

Master's thesis 2017:018
ISSN 1652-8557
Department of Applied Mechanics
Division of Dynamics
Chalmers University of Technology
SE-412 96 Göteborg
Sweden
Telephone: +46 (0)31-772 1000

Cover:
Volvo FH16 Truck [1], Engineering model of the Arc-spring friction system

Chalmers Reproservice
Göteborg, Sweden 2017

Simulation Models of Dual Mass Flywheels
Master's thesis in Applied Mechanics
DANIEL JOHANSSON
KIM KARLSSON
Department of Applied Mechanics
Division of Dynamics
Chalmers University of Technology

Abstract

Heavy duty trucks are faced with strict requirements regarding exhaust emissions and fuel efficiency. The demands are achieved through downsizing and downspeeding. This introduces torsional vibrations in the powertrain which, if not dealt with, will decrease life and comfort. One solution that deals with these vibrations is the Dual Mass Flywheel that absorbs the vibrations.

The goal of this thesis is to develop and verify different computational models of a Dual Mass Flywheel and in particular study how the friction between the arc-spring and the primary flywheel affects the system.

Modelling is done in Python using the Newmark-β method combined with Newton's method for numerical simulations. The same model is also created in AVL Excite for verification. The friction between the arc-spring and the primary flywheel channel is modelled using the Coulomb friction model or an inverse tangent function. It has been verified that the two computational models give similar results.

A method to approximate Coulomb friction has been developed in order to make the computational model more stable. The friction depends on both spring compression and centripetal force due to the rotation of the Dual Mass Flywheel. For a truck's operating speed the spring compression is the largest factor to frictional losses with current selection of geometrical and structural parameters. The results show that with low friction and low viscous damping resonance is not a significant problem even if it occurs at low engine speed. A study about the number of masses needed to solve the friction model have been performed. It is concluded that the friction moment has not converged using five spring masses. A method of achieving accurate results with few masses is presented.

For a final conclusion about the dynamics of the Dual Mass Flywheel, the developed computational models need to be validated using experimental data. Modifications of geometrical and structural parameters should be done to fit the experiments.

Keywords: Torsional Vibrations, Dual Mass Flywheel, Python, AVL Excite Timing Drive, Computational Models

Acknowledgements

First of all, we would like to express our gratitude to examiner Viktor Berbyuk who accepted our application for this master thesis and for all his support and guidance in this work. We also want to give a special thanks to our supervisors Lina Wramner and Håkan Johansson. Their guidance and supervisions in the modelling and the report writing made this thesis possible.

Furthermore, we would like to express our gratitude for AVL LIST GmbH who supplied Chalmers and our master thesis with licence for AVL Excite. This resulted in a great opportunity for us to learn the software and create two separate models. Last but not least, our sincere thanks to Volvo Group Trucks Technology in cooperation with Viktor Berbyuk who formulated this interesting and challenging thesis.

Daniel Johansson, Kim Karlsson, Göteborg, June 2017

Abbreviations and Nomenclature

Abbreviations

DMF	Dual Mass Flywheel
AVL	AVL Excite Timing Drive
DOF	Degrees Of Freedom
MDOF	Multi Degree Of Freedom
FBD	Free Body Diagram
RMS	Root Mean Square
RHS	Right Hand Side
BC	Boundary Condition

Nomenclature

ω	Angular velocity of the engine	[rad/s]
θ	Absolute rotational DOF	[rad]
φ	Angle between two masses of the arc-spring	[rad]
F_c	Centripetal force of the arc-spring	[N]
F_N	Normal force on the arc-spring	[N]
D	Diameter of the arc-spring	[m]
n	Engine speed	[rpm]
n_f	The order of the frequency data	[−]
T	Engine torque	[Nm]
μ	Friction of coefficient	[−]
F_f	Friction force for the arc-spring	[N]
T_f	Friction torque for the arc-spring	[Nm]
ω_{3rd}	Third order engine vibration	[rad/s]
ω_{max}	Maximum eigenfrequency	[rad/s]
J	Moment of inertia	[kgm^2]
m	Mass	[kg]
β	Newmark-β model parameter	[−]
γ	Newmark-β model parameter	[−]
ω_n	Natural eigenfrequency	[rad/s]
N	Number of DOFs of the arc-spring	[−]
λ	Phase shift angle harmonic motion	[rad]
ψ	Phase shift angle of the engine torque	[rad]

r	Radius out to the arc-spring	[m]
F_s	Spring compression force	[N]
T_s	Spring compression torque for the arc-spring	[Nm]
c	Torsional viscous damping coefficient	[Nms/rad]
h	Time step for, Newmark-β method	[s]
k	Torsional stiffness	[Nm/rad]
k_s	Translational stiffness	[N/m]
T_d	Viscous damping torque for the arc-spring	[Nm]

Contents

1 Introduction

The development of engines strives to constantly improve fuel efficiency. This is generally done by downsizing and downspeeding. Downsizing refers to that a larger engine is replaced by a smaller, which often includes fewer and smaller cylinders. Downspeeding refers to constructing the engine to produce maximal torque at lower engine speed [2], [3].

For the downsized/downspeeded engine to produce the same torque as before often the peak cylinder pressure is raised. This results in increased torsional vibrations in the powertrain which, if not dealt with, will decrease life of the powertrain and reduce comfort. Handling these vibrations can be done with many different concepts, one of them is the Dual Mass Flywheel (DMF). Input to the DMF is the varying torque from the crankshaft and output should ideally be a constant torque to the transmission. The DMF is constructed with two masses that are connected with one or more springs. The springs have the task to store energy peaks from the engine strokes and release the energy in a more constant matter.

1.1 Purpose

The purpose of this thesis is to investigate and learn more about the behaviour of the DMF when it is used in heavy duty trucks. In detail the purpose is to study the friction between the arc-spring and the channel on the primary flywheel. The study should include what the characteristics of the friction are at different engine loads and operating speeds. The goal of the thesis is to develop two different computational models, one in Python and one in AVL Excite Timing Drive (AVL), that can simulate the behaviour of the DMF and the friction that appears. The result from the two different models will be compared and analysed.

1.2 Limitations

This master thesis is constrained to 30 credits for two students, this translates to 1600 working hours. The most relevant delimitations of this thesis are listed below.

- Only torsional vibrations will be considered
- The system border will cover the whole DMF and the input shaft of the gearbox. How the torsional vibrations will affect the rest of the drivetrain will not be analysed
- Third engine order vibrations from the engine will mainly be considered
- The simulations will not be evaluated against any measurements, the different computational models will be evaluated against each other
- The model will not consider start-stop condition of the engine
- The clutch is assumed to have full contact, that is no slip between the clutch and the secondary flywheel
- Symmetry of the DMF is assumed, only one spring is modelled with the stiffness of both springs

1.3 Questions of research

To further specify the purpose of the thesis the following questions are formulated.

- What differences in DMF dynamics can be seen for different operating speeds of the engine?
- Are there any differences in the dynamics of the DMF for cars and trucks due to the difference in operating speed ranges?
- Which are the largest factors that contribute to the friction at the arc-spring?
- How many rotational degrees of freedom (DOF) are needed for the arc-spring in the DMF to ensure sufficient accuracy of the results?
- Is it necessary to have a more advanced friction model for the arc-spring or will the Coulomb friction model be enough?

2 Theory

In this chapter the most relevant theory is explained in different sections. Theory that has been used to define the different mathematical and computational models are included here.

2.1 Dual Mass Flywheel

The DMF consists of mainly three parts, two flywheels and a set of arc-springs, see Figure 2.1. In the figure there is also a forth component, the component with the purple details. This component is part of the secondary flywheel and can absorb energy through the purple pendulum masses or be modelled as rigid.

The primary flywheel is connected to the crankshaft and the secondary flywheel is connected to the clutch. In this manner the engine torque is transmitted directly to the primary flywheel, compressing the arc-spring and the arc-spring transfer the torque to the secondary flywheel. From the secondary flywheel, when the clutch is fully engaged, the torque is transferred to the gearbox. The two flywheels are constrained to rotate relative to each other with the stiffness of the arc-spring and damping coefficient. Resisting friction is also acting between the spring and the primary flywheel [4].

The main purpose for the DMF is to reduce rattle. Rattle comes from torsional vibrations created by the combustion engine. The DMF damps these vibrations before the torque is transmitted to the clutch and gearbox [4].

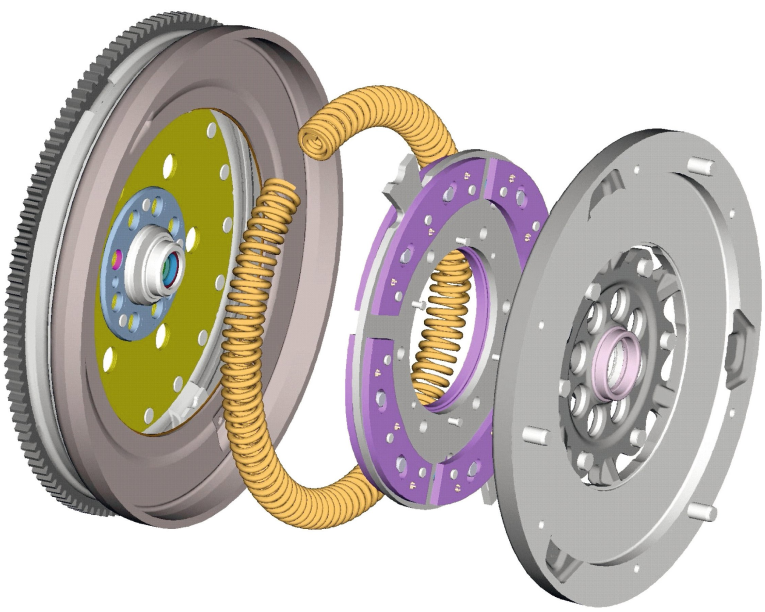

Figure 2.1: Exploded image of a Dual Mass Flywheel [5]

2.2 Engine dynamics

Truck engines such as Volvo's 16 litre engines have an operating speed around 800 to 2200 rpm [6]. Car engines have a larger operational speed interval of around 800 to 6000 rpm depending of the type of engine [7]. For DMF used in cars it is common that they have a so called inner damper in serial to the arc-spring in order to reduce vibrations that can appear at high engine speeds [4].

For six cylindrical combustion engines as Volvo uses in their trucks, three cylinders will fire during the first revolution of the engine crankshaft and the other three cylinders during the second revolution of the crankshaft. Thereby the combustion will create three vibration cycles at every revolution of the crankshaft. If the engine has a speed of ω the vibrations that will be transferred to the DMF will have a frequency of three times the frequency of the crankshaft as, $\omega_{3rd} = 3\omega$. This is known as third engine order vibrations.

2.3 Multi stage arc-spring

The arc-spring inside of the DMF, see Figure 2.1, can sometimes have stage characteristics. This means that during the first stage of relative displacement between the first and second flywheel the springs have a low stiffness. In the next stage a higher stiffness. A two stage characteristic can be achieved with two arc-springs, one with larger diameter and one with a smaller diameter. The smaller spring runs inside the larger one and one of the springs is shorter than the other. Multiple stages can also be achieved through linear springs connected in series [8].

A correct design of the stiffness in the stages can position the resonance frequencies of the drive train below below the frequency of third engine order at idle speed and above the frequency of third engine order at maximal engine speed. This eliminates the risk of resonance and it is still possible to transmit a high torque [8].

2.4 Friction modelling of the arc-spring

A way of modelling the arc-spring is to divide it into N number of masses with equal mass, m_i, for $i = 1, .., N$, where i is the rotational DOF of the arc-spring. The masses are connected with $N + 1$ number of spring segments and the friction force that will act on the masses will depend on both centripetal force and spring compression [9]. In some models the frictional force includes a constant bias force, F_{bias} [9], [10].

The contact between the primary flywheel and the arc-spring will contribute to friction and energy dissipation. This requires a friction model that incorporates this behaviour [10].

To model the hysteresis and nonlinear phenomenon of the arc-spring due to friction one way is to use the Coulomb friction model. With Coulomb friction model there is only need of one friction coefficient μ [11]. To capture a more complex frictional behaviour an other friction model could be needed, such as LuGre friction model. This model requires some model parameters obtained by experiments or estimation. This model is more accurate than Coulomb friction model regarding high accelerations, specifically fast sign changes of the velocity [11].

2.5 Newmark - β method

This is a discrete integration method for solving a differential equation. The benefit of the Newmark - β method is that it is unconditionally stable given that the time step, h, is chosen according to

$$h \leq \frac{2}{\omega_{max}} \tag{2.1}$$

Here ω_{max} denotes the maximal eigenfrequency of the system. The derivation of the method is presented below [12].

The multi-degree of freedom (MDOF) problem of second order on matrix form for the time step (n+1) can be expressed as

$$\underline{\boldsymbol{M}}\ddot{\boldsymbol{\theta}}_{n+1} + \underline{\boldsymbol{C}}\dot{\boldsymbol{\theta}}_{n+1} + \underline{\boldsymbol{K}}\boldsymbol{\theta}_{n+1} = \boldsymbol{p}_{n+1} \tag{2.2}$$

The initial acceleration (for n=0) is determined by Eq. (2.3) assuming that the initial velocity and displacement are assumed to be known.

$$\ddot{\boldsymbol{\theta}}_0 = \underline{\boldsymbol{M}}^{-1}[\boldsymbol{p}_0 - \underline{\boldsymbol{C}}\dot{\boldsymbol{\theta}}_0 - \underline{\boldsymbol{K}}\boldsymbol{\theta}_0] \tag{2.3}$$

The velocity (first derivative) can be expressed as Eq. (2.4) and the displacement (zero derivative) as Eq. (2.5).

$$\dot{\boldsymbol{\theta}}_{n+1} \approx \dot{\boldsymbol{\theta}}_n + h[(1-\gamma)\ddot{\boldsymbol{\theta}}_n + \gamma\ddot{\boldsymbol{\theta}}_{n+1}] \tag{2.4}$$

$$\boldsymbol{\theta}_{n+1} \approx \boldsymbol{\theta}_n + h\dot{\boldsymbol{\theta}}_n + \frac{h^2}{2}[(1-2\beta)\ddot{\boldsymbol{\theta}}_n + 2\beta\ddot{\boldsymbol{\theta}}_{n+1}] \tag{2.5}$$

Here is assumed that $2\beta \geq \gamma \geq \frac{1}{2}$. Note that, this choice of parameters, yields the Constant Average Acceleration Method which is unconditionally stable [12].

The new acceleration, $\ddot{\boldsymbol{\theta}}_{n+1}$, can be determined by inserting the Eqs. (2.4) and (2.5) into Eq. (2.2), which ends up as Eq. (2.6).

$$\ddot{\boldsymbol{\theta}}_{n+1} = [\underline{\boldsymbol{M}} + \gamma\underline{\boldsymbol{C}} + \beta h^2\underline{\boldsymbol{K}}]^{-1}\left[\boldsymbol{p}_{n+1} - \underline{\boldsymbol{K}}\boldsymbol{\theta}_n - (\underline{\boldsymbol{C}} + h\underline{\boldsymbol{K}})\dot{\boldsymbol{\theta}}_n - \left(h(1-\gamma)\underline{\boldsymbol{C}} + \frac{h^2}{2}(1-2\beta)\underline{\boldsymbol{K}}\right)\ddot{\boldsymbol{\theta}}_n\right] \tag{2.6}$$

The new velocity, $\dot{\boldsymbol{\theta}}_{n+1}$, and the displacement, $\boldsymbol{\theta}_{n+1}$, can then be determined by the Eqs. (2.4) and (2.5).

2.6 Newton's - method

Newton's method is used to approximate the solution for a non-linear function or a set of non-linear functions, $f(\theta)$. Functional value of zero is sought.

Initially the solution to a time step is guessed as θ_0. The time step is updated with Eq. (2.7).

$$\theta_{k+1} = \theta_k - J^{-1} f(\theta_k) \tag{2.7}$$

where J is the Jacobian of f.

$$J(\theta_k) = \nabla f(\theta_k)$$

The iterations for each time step are performed according to Eq 2.7. Iteration stops when $||J^{-1} f(\theta_k)|| < tolerance$ and the initial guess for the next timestep becomes $\theta_0^n = \theta_k^{n-1}$, [13].

2.7 Eigenvalues

In general the natural undamped eigenvalues are calculated based on the following derivation. It will start with the MDOF problem

$$\underline{\boldsymbol{M}}\ddot{\boldsymbol{\theta}} + \underline{\boldsymbol{K}}\boldsymbol{\theta} = \boldsymbol{P} \tag{2.8}$$

It will be assumed that the natural frequencies do not significantly depend on the damping $\underline{\boldsymbol{C}}$ and therefore only consider the free vibrations. This is an accurate assumption when the damping coefficients are small.

Harmonic motion is then assumed which gives

$$\theta_i(t) = U_i cos(\omega_n t - \lambda) \tag{2.9}$$

The second derivative of the harmonic motion can be expressed as

$$\ddot{\theta}_i(t) = -U_i \omega_n^2 cos(\omega_n t - \lambda) \tag{2.10}$$

The second derivative of the harmonic motion in Eq. (2.10) is then inserted in the MDOF problem in Eq. (2.8). It will then end up with the following equation expressed on matrix form

$$\left[\underline{\boldsymbol{K}} - \omega_n^2 \underline{\boldsymbol{M}}\right]\boldsymbol{U} = \boldsymbol{0} \tag{2.11}$$

The eigenvalues for the system can then be computed using the following equation

$$det(\underline{\boldsymbol{K}} - \omega_n^2 \underline{\boldsymbol{M}}) = 0 \tag{2.12}$$

2.8 Engine torque translated from frequency domain

The engine torque can be computed as a Fourier series expansion, based on data from the frequency domain. Then it can be converted into the time domain considering the torque to be a periodic load. A general periodic load can be expressed as a complex Fourier series

$$p(t) = \sum_{x=-\infty}^{\infty} B_x e^{2\pi i x \frac{t}{T_p}} \tag{2.13}$$

T_p represents the period, which is $\frac{4\pi}{\omega}$ for four-stroke six cylinder engines. The constant B_x are complex and $B_{-x} = B_x^*$. This means that Eq. (2.13) is equivalent to Eq. (2.14)

$$p(t) = REAL\Big(B_0 + \sum_{x=1}^{\infty} 2B_x e^{2\pi i x \frac{t}{T_p}}\Big) \tag{2.14}$$

The torque, $T(t)$, transferred to the primary flywheel can then be expressed as

$$T(t) = REAL\Big(B_0 + \sum_{x=1}^{\infty} 2B_x e^{2\pi i x \frac{t}{T_p}}\Big) = REAL\Big(P_0 + \sum_{x=1}^{\infty} P_x e^{2\pi i x \frac{t}{T_p}}\Big) \tag{2.15}$$

Here $P_0 = B_0 = 0$ and $P_x = B_x$ for $x > 0$, where P_x is a complex number. The values of the torques, P_x for $x = 0, .., 24$, have been provided from Volvo for a couple of engine speeds [14] and represent the torque before the flywheel in a typical heavy-duty truck powertrain. The engine torque, $T(t)$, for any engine speed for the period $\frac{4\pi}{\omega}$ can be determined as

$$T(t) = REAL\Big(\sum_{x=0}^{24} P_x e^{i \frac{x}{2} \omega t}\Big) \tag{2.16}$$

The engine torque, $T_\theta(\theta)$, as a function of the revolution of the crankshaft can then be computed as

$$T_\theta(\theta) = REAL\Big(\sum_{x=0}^{24} P_x e^{i \frac{x}{2} \theta}\Big) \tag{2.17}$$

Linear interpolation can be used to compute the interpolated engine torque, $T_{\theta,ip}(\theta)$, as a function of the revolution of the crankshaft, for any engine speed, n_{ip}, in the total range of interest.

$$\frac{n_{ip} - n_0}{T_{\theta,ip}(\theta) - T_{\theta,0}(\theta)} = \frac{n_1 - n_0}{T_{\theta,1}(\theta) - T_{\theta,0}(\theta)} \tag{2.18}$$

Thereby the wanted engine torque, $T_{\theta,ip}(\theta)$, for the engine speed, n_{ip}, can be computed with Eq. (2.19). The engine speed n_{ip} for the interpolated engine torque, $T_{\theta,ip}(\theta)$, is in between the engine speeds n_0 and n_1.

$$T_{\theta,ip}(\theta) = \frac{T_{\theta,1}(\theta) - T_{\theta,0}(\theta)}{n_1 - n_0}(n_{ip} - n_0) + T_{\theta,0}(\theta) \tag{2.19}$$

3 Method

Initially a literature study of the DMF was performed. The study included theoretical studies of the torsional vibration from the engine and its impact on the DMF at different operating speeds. Different types of concepts of DMF were studied to enable to create a first engineering model over the system.

3.1 Model 1 - Linear spring system

This model represents the very basics of a DMF. The model has two degrees of freedom, the primary- and secondary flywheel. In the end the relative displacement, velocity and acceleration between these can be observed. All systems structural parameters are assumed to be constant.

The system is initially at stationary speed and zero displacement. It is loaded with the engine torque on the primary flywheel and the secondary mass is bounded by a constant motion from the input shaft of the gearbox.

3.1.1 Engineering model

The DMF was modelled with two masses representing the primary and the secondary flywheel, which have the moments of inertia J_{pri} and J_{sec} respectively. The connection between the flywheels is modelled with a spring with the equivalent stiffness, k_{eq}, and a damper with the equivalent damping, c_{eq}. The system border covers the DMF and the clutch/input shaft of the gearbox, which is modelled with a stiffness k_{is} and a damping c_{is}. The torque that is applied on the input shaft is denoted as T_{gear}. The torque that is transferred from the engine to the flywheel is denoted as T_{eng}, which considers third order engine vibrations. The resulted engineering model is depicted in Figure 3.1.

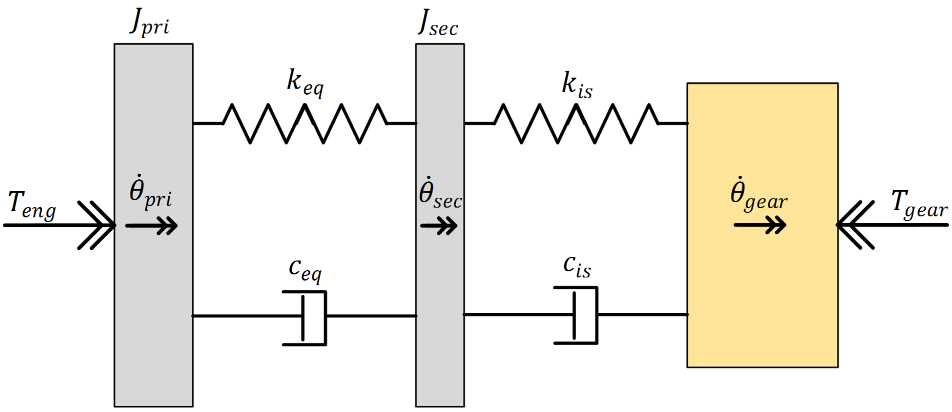

Figure 3.1: Linear spring model of the DMF

This model can also be reduced further so that the system borders consider the input torque from the engine to the primary flywheel to the output torque from the secondary flywheel. The counter torque from the gearbox, T_{gear}, is applied directly to the secondary flywheel, depicted in Figure 3.2. This is similar to have a rigid axle between the flywheel and the gearbox without damping.

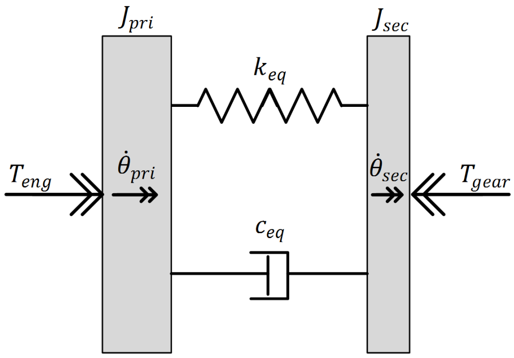

Figure 3.2: Linear spring model of the DMF without the input shaft of the gearbox

The structural parameters used for the engineering model, see Figure 3.1, are presented in Table 3.1. Here three sets of structural parameters A, B and C are presented. The structural parameters A are from [15] (where the equivalent damping is increased to $c_{eq} = 300$ Nms/rad) and the structural parameters B are estimated to represent a DMF for trucks. Structural parameters C have a low damping in order to not hide any dynamic phenomena in the frictional modelling.

Table 3.1: DMF structural parameters

	J_{pri} [kgm^2]	J_{sec} [kgm^2]	k_{eq} [Nm/rad]	k_{is} [Nm/rad]	c_{eq} [Nms/rad]	c_{is} [Nms/rad]
A	1.8	0.6	20000	11000	300	10
B	0.9	1.75	12732	100000	300	10
C	0.9	1.75	12732	100000	5	10

3.1.2 Mathematical model

Newton's second law applied on the model

The Newton's second law of rotational motion was applied on the primary flywheel Eq. (3.1) and the secondary flywheel Eq. (3.2), using the free body diagram (FBD) method of the engineering model in Figure 3.1.

$$J_{pri}\ddot{\theta}_{pri} + c_{eq}(\dot{\theta}_{pri} - \dot{\theta}_{sec}) + k_{eq}(\theta_{pri} - \theta_{sec}) = T_{eng} \tag{3.1}$$

$$J_{sec}\ddot{\theta}_{sec} + c_{eq}(\dot{\theta}_{sec} - \dot{\theta}_{pri}) + c_{is}(\dot{\theta}_{sec} - \dot{\theta}_{gear}) + k_{eq}(\theta_{sec} - \theta_{pri}) + k_{is}(\theta_{sec} - \theta_{gear}) = 0 \tag{3.2}$$

This can be rewritten on matrix form as

$$\begin{bmatrix} J_{pri} & 0 \\ 0 & J_{sec} \end{bmatrix} \begin{bmatrix} \ddot{\theta}_{pri} \\ \ddot{\theta}_{sec} \end{bmatrix} + \begin{bmatrix} c_{eq} & -c_{eq} \\ -c_{eq} & c_{eq} + c_{is} \end{bmatrix} \begin{bmatrix} \dot{\theta}_{pri} \\ \dot{\theta}_{sec} \end{bmatrix} + \begin{bmatrix} k_{eq} & -k_{eq} \\ -k_{eq} & k_{eq} + k_{is} \end{bmatrix} \begin{bmatrix} \theta_{pri} \\ \theta_{sec} \end{bmatrix} = \begin{bmatrix} T_{eng} \\ c_{is}\dot{\theta}_{gear} + k_{is}\theta_{gear} \end{bmatrix} \tag{3.3}$$

The input torque to the flywheel, T_{eng}, was estimated as a sine load

$$T_{eng}(t) = T_0 + T_A sin(\omega_{3rd}t + \psi) = 300 + 500 sin(\omega_{3rd}t) \tag{3.4}$$

here the frequency, ω_{3rd}, is the third engine order vibration, that is three times the angular velocity of the crankshaft, $\omega_{3rd} = 3\omega$. The angular velocity of the crankshaft was computed as $\omega = \frac{2\pi n}{60}$, where n is the engine speed rpm.

Eigenvalues

The natural undamped eigenvalues for the system were computed using Eq. (2.12) presented in section 2.7. These were computed so that the possible resonance phenomenon could be explained and foreseen in the result.

Flywheel torque converted from frequency domain

To compute the realistic engine torques, $T(t)$, Eq. (2.16) was used presented in section 2.8, using given data for torque applied on the primary flywheel at certain engine speeds [14]. The engine torques, $T_\theta(\theta)$, as a function of the revolution of the crankshaft were computed using Eq. (2.17). Linear interpolation was performed in the code [14] since the provided data had a specific amount of engine speeds. The engine torque could then be computed for any engine speed in the total range of interest.

3.1.3 Computational model

Python

To solve the second order differential equation Eq. (3.3) the Newmark - β method was implemented in Python [16]. For the derivation of the Newmark - β method, see section 2.5.

AVL

The first model in AVL [17] was implemented according to Figure 3.3. The load data was imported from csv files with 200 time steps per load cycle. Either the sine or the realistic engine torque can be selected. Spring1 has stiffness k_{eq} and viscous damping c_{eq} from Table 3.1. IS_spring has k_{is} as stiffness and c_{is} as viscous damping. Initially all masses rotate with the engine speed. The flywheels are unconstrained rotational DOF and the gearbox was constrained to the engine speed. All the parameters used can be seen in Appendix A.1

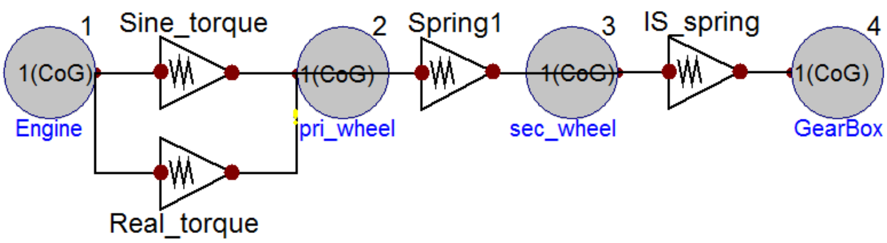

Figure 3.3: Graphical model AVL, linear spring system

3.1.4 Results

The eigenvalues for Model 1 are calculated using Eq. (2.12) for the structural parameters A and B in Table 3.1. The natural undamped eigenfrequencies are presented in Table 3.2. The second eigenfrequency is located around the engine speed of 800 rpm for both sets of structural parameters. Hence the torsional vibrations dynamics $(\theta_{pri} - \theta_{sec})$ of the system is expected to be high for the engine speed 800 rpm if the damping coefficient is low. With a high damping coefficient the calculated eigenfrequencies will be overestimated and resonance should not be expected.

Table 3.2: Undamped eigenfrequencies for the linear spring system

Eigenmode	1	2
Structural parameters A, $\frac{\omega_n}{3}$ [rpm]	186.49	775.43
Structural parameters B, $\frac{\omega_n}{3}$ [rpm]	351.24	820.15
Structural parameters A, ω_{3rd} [Hz]	9.32	38.77
Structural parameters B, ω_{3rd} [Hz]	17.56	41.01

The systems torsional vibration ($\theta_{pri} - \theta_{sec}$) for the Python model using the Newmark-β method presented in section 2.5 was solved and obtained. The same structural parameters as in the previous MSc project [15] (structural parameters A) were used, gathered in Table 3.1. The different load cases that have been used in this section are Eq. (3.4) and (2.16). The results of the simulations are illustrated in Figure 3.4 which can be verified with the previous work [15]. The damping coefficient is relatively low, which means that the eigenfrequencies are accurate.

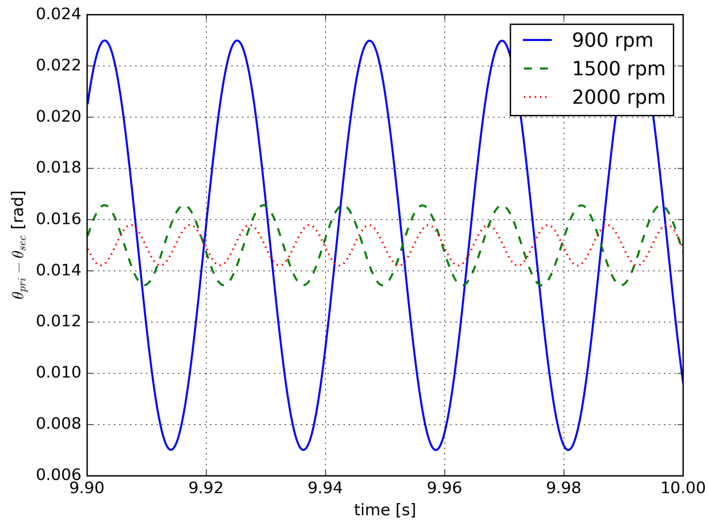

Figure 3.4: Model 1, solved with structural parameters from [15], sine load

It was decided that the engine speeds, 800, 1400 and 2000 rpm, are going to be used and the corresponding simulation results are presented in Figure 3.5. This ensures that the result for 0.1 second yields exactly four, seven and ten complete load cycles respectively. Further calculations of root mean square (RMS) values of the system's response will then have better accuracy without any modifications to the calculations.

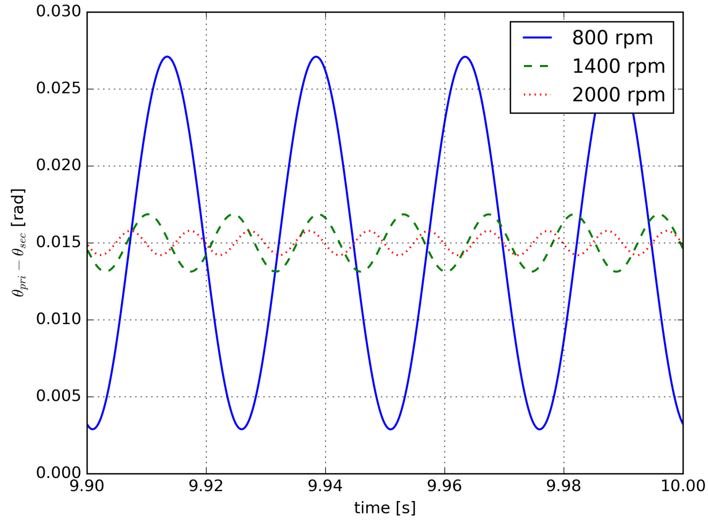

Figure 3.5: Model 1, solved with structural parameters A in Table 3.1, sine load

The realistic engine torque, $T_\theta(\theta)$, was computed using Eq. (2.17) presented in section 2.8. The results for two revolutions of the crankshaft for the three engine speeds, 800, 1400 and 2000 rpm are presented in Figure 3.6.

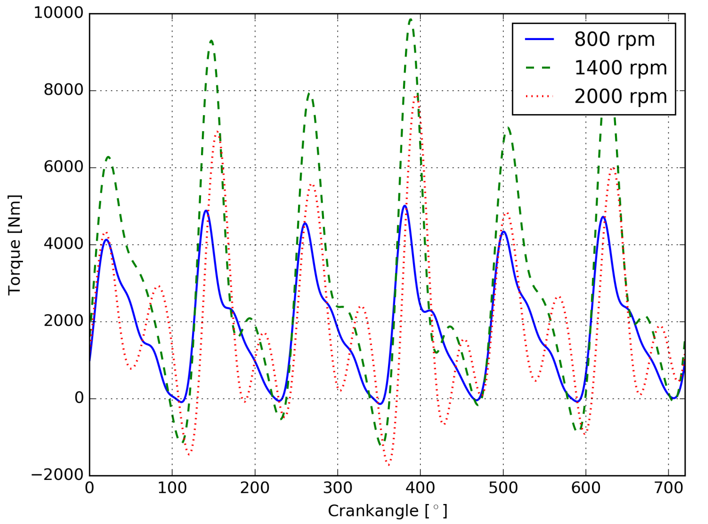

Figure 3.6: Engine torques for different speeds

The flywheel torques computed for all the engine speeds, 800, 1000, 1400, 1600, 1800 and 2000 rpm are shown in Figure 3.7.

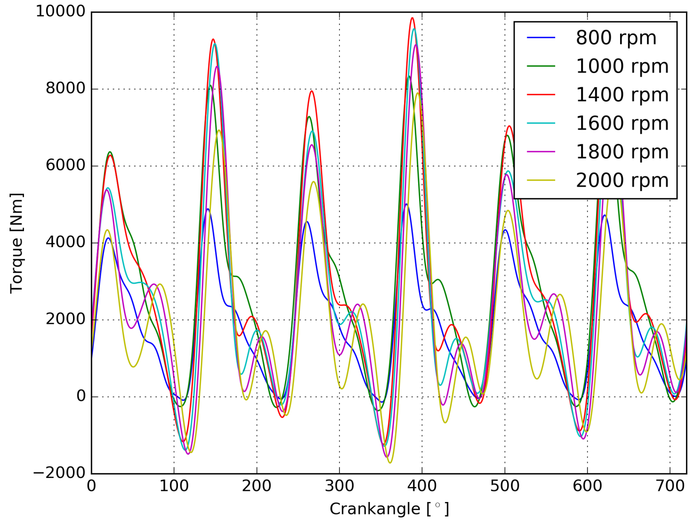

Figure 3.7: Engine torques for all the different speeds

The flywheel torques computed for the three engine speeds, 800, 900 and 1000 rpm are shown in Figure 3.8. Here the interpolated flywheel torque, $T_{\theta,ip}(\theta)$, for the engine speed, 900 rpm, was computed using Eq. (2.19) presented in section 2.8.

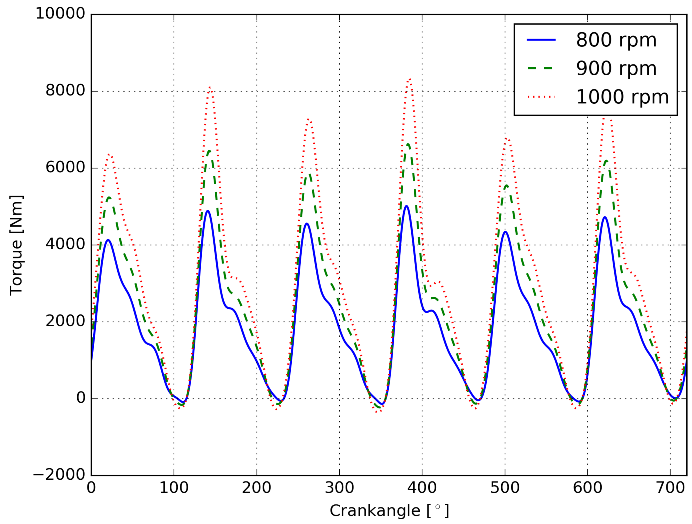

Figure 3.8: Linear interpolated engine torque

To evaluate the Python- and AVL models, the systems torsional vibration dynamics ($\theta_{pri} - \theta_{sec}$) have been obtained and compared. The results of the simulations obtained for the two computational models using the structural parameters A in Table 3.1 and the sine load computed from Eq. (3.4) are shown in the Figures 3.9 and 3.10. The result of the simulations when changing the sine load to the realistic engine torque computed from Eq. (2.16) are shown in the Figures 3.11 and 3.12.

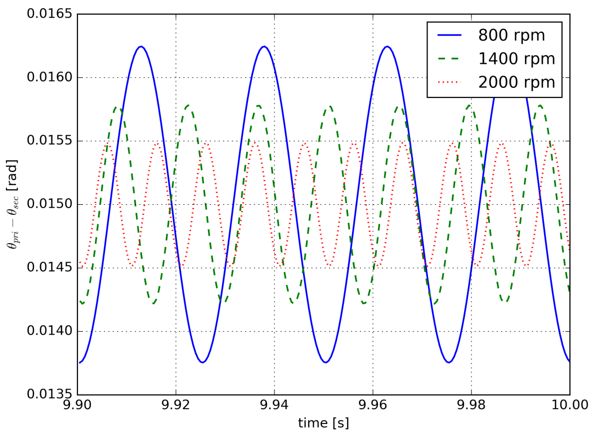

Figure 3.9: Linear model, sine load, Python

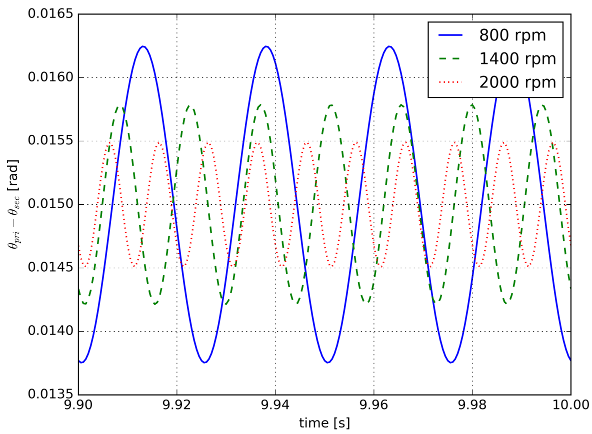

Figure 3.10: Linear model, sine load, AVL

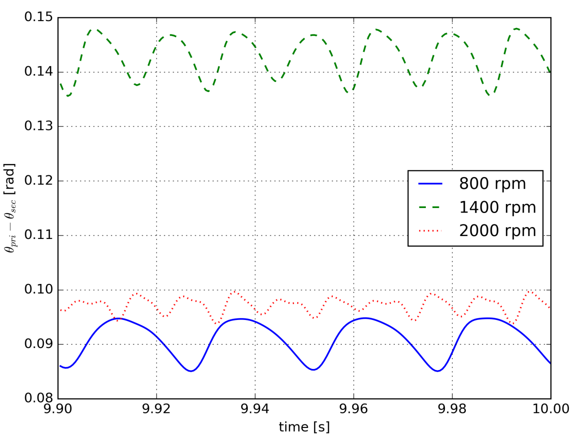

Figure 3.11: Linear model, realistic load, Python

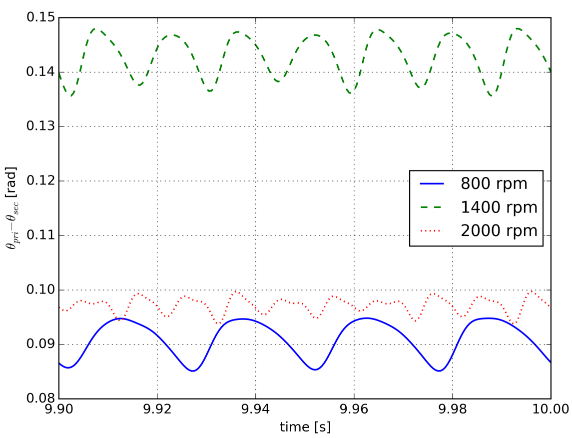

Figure 3.12: Linear model, realistic load, AVL

The relative angular displacement for the engine speed, 800 rpm, is reduced in Figure 3.9 due to the increased damping. The equivalent damping, c_{eq}, was increased to $c_{eq} = 300$ Nms/rad as in Table 3.1. This can be compared to the results in Figure 3.5, where the damping used was $c_{eq} = 30$ Nms/rad from [15].

Analysis of the curves in the Figures 3.9-3.12 shows that the DMF torsional vibration dynamics are approximately the same for the two computational models. The RMS values for each curve are gathered in Table 3.3, which shows the difference of the solutions between the computational models.

Table 3.3: RMS values for the linear spring model, structural parameters A

Engine speed [rpm]	800		1400		2000	
Software	Python	AVL	Python	AVL	Python	AVL
RMS sine load	0.01502617	0.01502585	0.01501053	0.01501024	0.01500431	0.01500402
RMS realistic load	0.09105376	0.09104965	0.14294710	0.14293847	0.09720514	0.09720166

The result of the simulations obtained for the two computational models, using the structural parameters B in Table 3.1 and the sine load computed from Eq. (3.4) are presented in the Figures 3.13 and 3.14. The result of the simulations when changing the sine load to the realistic engine torque computed from Eq. (2.16) are presented in the Figures 3.15 and 3.16.

Analysis of the curves in the Figures 3.13-3.16 shows that the DMF torsional vibration dynamics are approximately the same for the two computational models. The RMS values for each curve are gathered in Table 3.4, which shows the difference of the solution between the computational models.

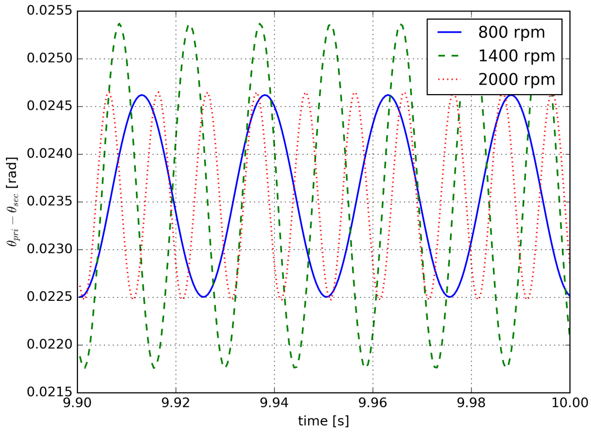

Figure 3.13: Linear model, sine load, Python

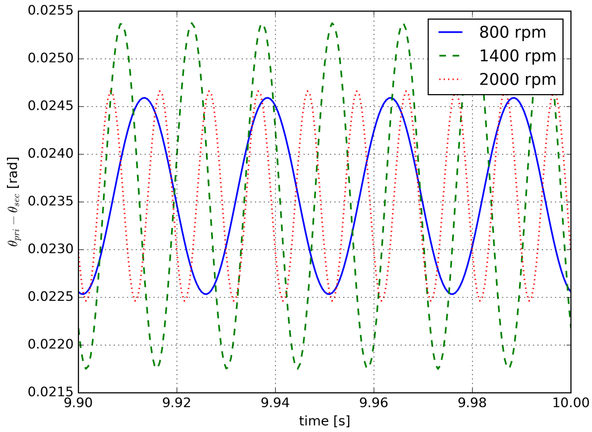

Figure 3.14: Linear model, sine load, AVL

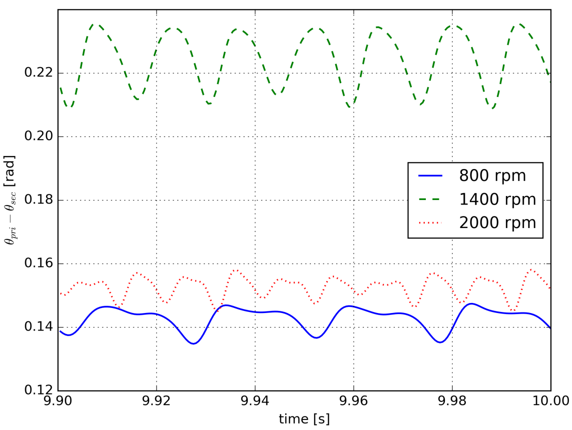

Figure 3.15: Linear model, realistic load, Python

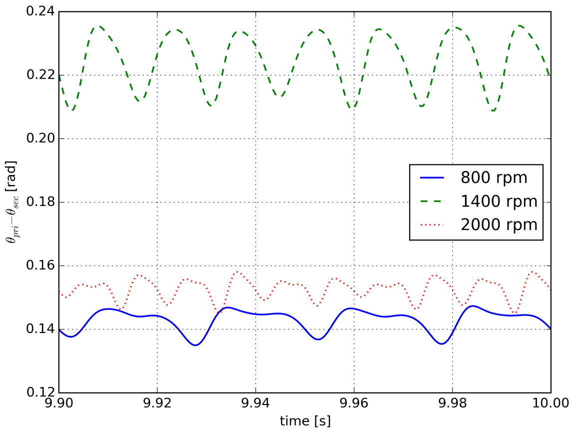

Figure 3.16: Linear model, realistic load, AVL

Table 3.4: RMS values for the linear spring model, structural parameters B

Engine speed [rpm]	800		1400		2000	
Software	Python	AVL	Python	AVL	Python	AVL
RMS sine load	0.02357511	0.02357387	0.02359782	0.02359747	0.02357589	0.02357552
RMS realistic load	0.14297873	0.14297097	0.22462741	0.22461807	0.15269036	0.15268378

Analysis of the systems relative angular displacement ($\theta_{pri} - \theta_{sec}$) for the Python- and AVL models have been compared and evaluated using the two computational models for different structural parameters and engine/flywheel torques. The evaluation between the models showed that the solutions were approximately the same. Conclusion about the correlation between the models can be drawn through visual inspections of Figures 3.9-3.16 together with the RMS values in Tables 3.3 and 3.4.

3.2 Model 2 - Two stage spring system

This model is an extension of Model 1 presented in section 3.1. Implementation of a step wise linear behaviour, see section 2.3, will be performed to the linear spring k_{eq}. The stiffness behaviour is depicted in Figure 3.1.

3.2.1 Engineering model

The addition to this model from the engineering model presented in section 3.1.1 is that the stiffness k_{eq} is a function of the relative angular displacement ($\theta_{pri} - \theta_{sec}$) of the two flywheels. The stiffness is doubled when the relative angular displacement is larger than ξ. In this case ξ was set to 0.75°, see Eq. (3.5).

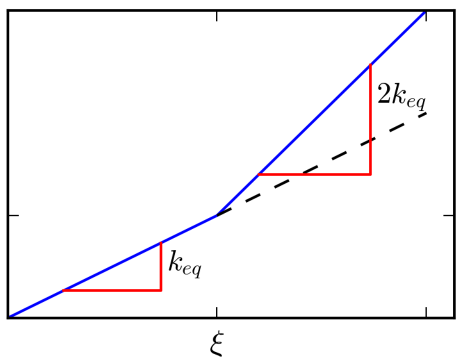

Figure 3.17: Characteristic of the two stage spring

$$k_{ms}(\theta) = \begin{cases} k_{eq} & \text{if } |\theta_{pri} - \theta_{sec}| < \xi \\ 2k_{eq} & \text{else} \end{cases} \tag{3.5}$$

The parameter that increases the stiffness and the parameter that determines when the stiffness should increase is chosen just to make the mathematical model non-linear. It has not been investigated further how these parameters affect the system.

3.2.2 Mathematical model

The mathematical model is similar to the mathematical model presented in section 3.1.2 with the new definition of k_{ms}. Eq. (3.3) is rewritten to Eq. (3.6).

$$\begin{bmatrix} J_{pri} & 0 \\ 0 & J_{sec} \end{bmatrix} \begin{bmatrix} \ddot{\theta}_{pri} \\ \ddot{\theta}_{sec} \end{bmatrix} + \begin{bmatrix} c_{eq} & -c_{eq} \\ -c_{eq} & c_{eq} + c_{is} \end{bmatrix} \begin{bmatrix} \dot{\theta}_{pri} \\ \dot{\theta}_{sec} \end{bmatrix} + \begin{bmatrix} k_{eq} & -k_{eq} \\ -k_{eq} & k_{eq} + k_{is} \end{bmatrix} \begin{bmatrix} \theta_{pri} \\ \theta_{sec} \end{bmatrix} = \begin{bmatrix} T_{eng} \\ c_{is}\dot{\theta}_{gear} + k_{is}\theta_{gear} \end{bmatrix} - \begin{bmatrix} k_{eq}\Delta\theta \\ -k_{eq}\Delta\theta \end{bmatrix} \tag{3.6}$$

Here $k_{eq}\Delta\theta$ is the force generated by the compression greater than ξ, see Figure 3.17. This force exists only when the compression is sufficiently large, hence the model has a non-linear behaviour.

$$\Delta\theta = \begin{cases} 0 & \text{if } |\theta_{pri} - \theta_{sec}| < \xi \\ \theta_{pri} - \theta_{sec} - \xi & \text{if } \theta_{pri} - \theta_{sec} > \xi \\ -\theta_{pri} + \theta_{sec} + \xi & \text{if } \theta_{pri} - \theta_{sec} < -\xi \end{cases} \tag{3.7}$$

3.2.3 Computational model

Python

Newton's method, see section 2.6, was used to solve the non-linear system. The exact theory that was used within the software is uncertain since the function fsolve in Python that was used is within the scipy module. But the basic theory of Newton's method explains what needs to be done to the model in order for it to converge.

AVL

In addition to the linear model in AVL the stiffness between the two flywheels was divided into two springs. k1_stage1 is identical to the linear model, and k1_stage2 is a spring with the stiffness, k_{eq}, but with a gap of 0.75° in both directions of the spring compression. In this manner, the two stages will create a spring that has double stiffness when the deformation is larger than 0.75°. For more detailed information of the parameters used, see Appendix A.2.

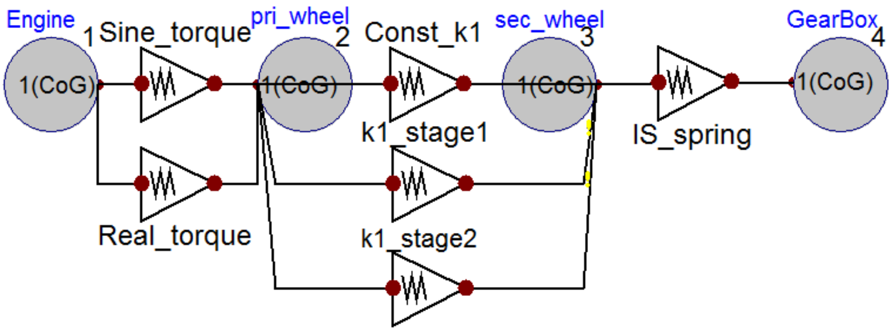

Figure 3.18: Graphical model AVL, Two stage spring

3.2.4 Result

The undamped eigenvalues for this model for vibrations in the region of lower stiffness are the same as for Model 1 in Table 3.2 computed using Eq. (2.12). This is expected, since the engineering model and the structural parameters are the same.

To evaluate the Python- and AVL models for the two stage spring system, the torsional vibrations ($\theta_{pri} - \theta_{sec}$) have been obtained and compared. The results of the simulations using the structural parameters A in Table 3.1 and the sine engine load, determined by Eq. (3.4) are shown in Figures 3.19 and 3.20. The results when changing the sine load to the realistic engine torque determined from Eq. (2.16) are shown in Figures 3.21 and 3.22.

Analysis of the curves in the Figures 3.19-3.22 shows that the DMF torsional vibration dynamics are approximately the same for the two computational models. The RMS values for each curve are presented in Table 3.5, which shows the difference of the solution between the computational models.

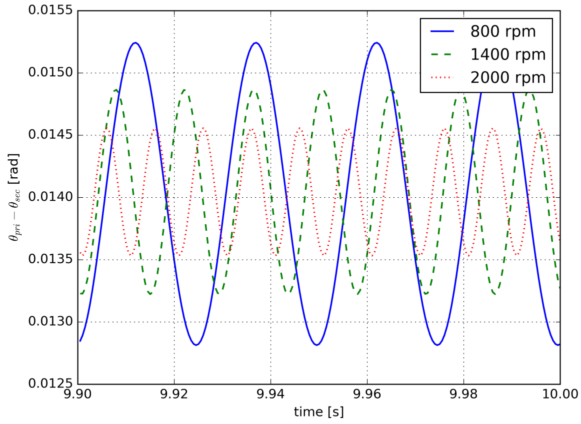

Figure 3.19: Two stage spring model, sine load, Python

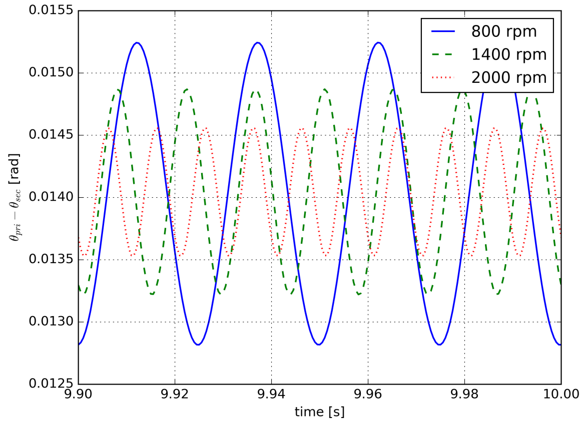

Figure 3.20: Two stage spring model, sine load, AVL

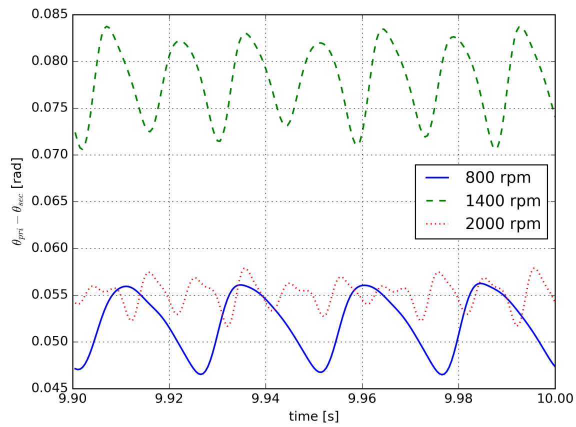

Figure 3.21: Two stage spring model, realistic load, Python

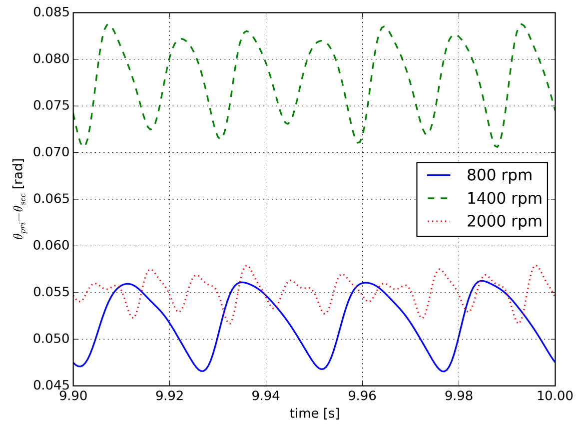

Figure 3.22: Two stage spring model, realistic load, AVL

Table 3.5: RMS values for the Two stage spring system, structural parameters A

Engine speed [rpm]	800		1400		2000	
Software	Python	AVL	Python	AVL	Python	AVL
RMS sine load	0.01405128	0.01405227	0.0140573	0.01405703	0.01404998	0.01404968
RMS realistic load	0.05214866	0.05214608	0.0780838	0.07807914	0.05516676	0.05516543

The result of the simulations using the structural parameters B in Table 3.1 and the sine load computed from Eq. (3.4) are shown in the Figures 3.23 and 3.24. The result of the simulations when changing the sine load to the realistic engine torque determined from Eq. (2.16) are shown in the Figures 3.15 and 3.16.

Analysis of the curves in the Figures 3.23-3.26 shows that the DMF torsional vibration dynamics are approximately the same for the two computational models. The RMS values for each curve are gathered in Table 3.6, which shows the difference of the solution between the computational models.

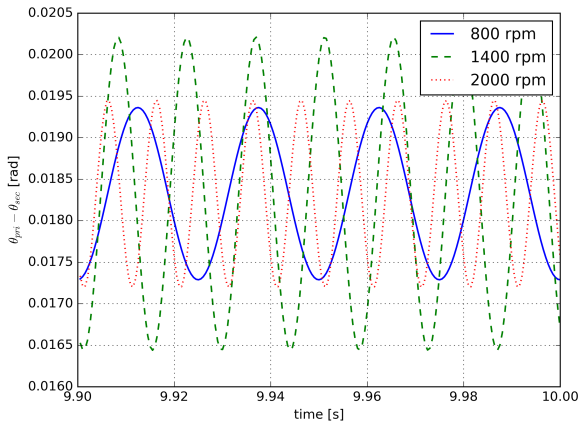

Figure 3.23: Two stage spring model, sine load, Python

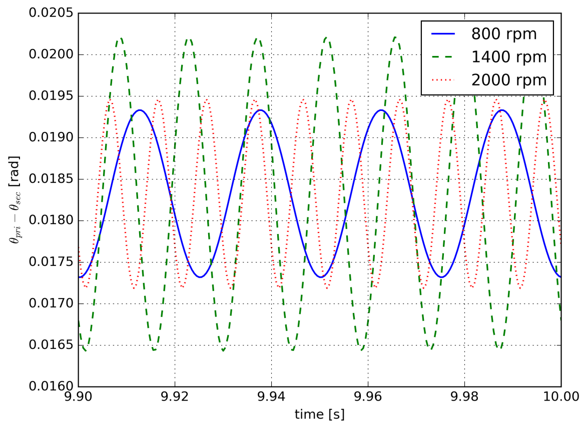

Figure 3.24: Two stage spring model, sine load, AVL

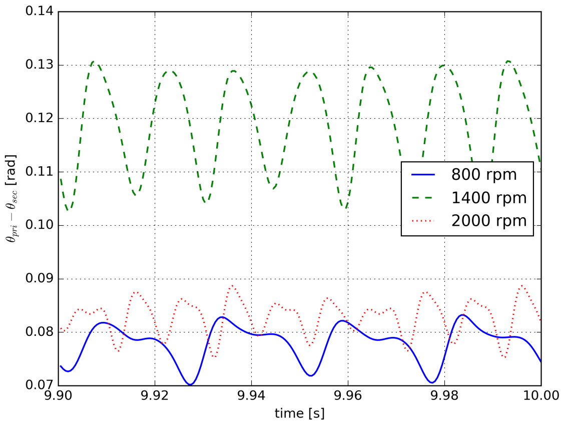

Figure 3.25: Two stage spring model, realistic load, Python

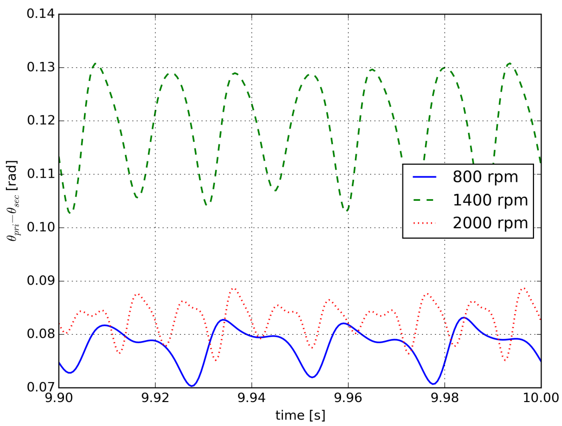

Figure 3.26: Two stage spring model, realistic load, AVL

Studying the amplitudes, for $n = 800$ rpm, of Figures 3.19-3.26 in comparison to Figures 3.9-3.16 a close similarity is observed. According to the second eigenfrequency in Table 3.2 the amplitudes in Figures 3.19-3.26 should not be in the resonance and have a significantly lower amplitude. This is not the case since the damping coefficient of structural parameters A and B (300 Nms/rad) moves the actual eigenfrequency well under 800 rpm, hence the similarities in amplitudes between the models.

Table 3.6: RMS values for the Two stage spring system, structural parameters B

Engine speed [rpm]	800		1400		2000	
Software	Python	AVL	Python	AVL	Python	AVL
RMS sine load	0.0183414	0.01834009	0.01837516	0.01837505	0.01834413	0.01834395
RMS realistic load	0.07808801	0.07808173	0.1190769	0.11907355	0.08294493	0.08294185

The systems relative angular displacement $(\theta_{pri} - \theta_{sec})$ for the Python- and AVL models have been compared and evaluated using the two computational models. The different structural parameters and engine/flywheel torques were used in the computational model in the same way as for model 1. The evaluation between the models showed that the solutions are approximately the same. Conclusion about the correlation between the models can be drawn through visual inspections of the Figures 3.19-3.26 together with the RMS values in Tables 3.5 and 3.6.

3.3 Model 3 - Arc-spring friction model

In this model, friction will be implemented to the DMF between the arc-spring and the channel of the primary flywheel. The friction will induce a non-linear behaviour to the system.

3.3.1 Engineering model

The DMF was modelled with two masses representing the primary and the secondary flywheel, which have the moments of inertia J_{pri} and J_{sec} respectively as for the linear spring system. The engine torque will be transferred from the primary to the secondary flywheel via the arc-spring. The arc-spring is divided into N number of masses with equal mass, m_i, $i = 1, .., N$. The masses are connected with $N + 1$ number of spring segments, k_j, $j = 1, .., N + 1$. The friction torque, $T_{f,i}$, that will act on the masses is modelled to depend on both centripetal force and spring compression. The engineering model for the system is depicted in Figure 3.27.

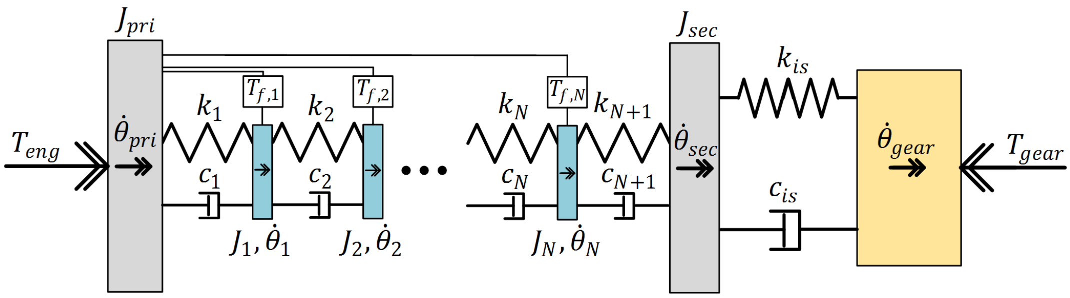

Figure 3.27: Engineering model with N number of masses of the arc-spring

The engineering model for an arc-spring with five masses with equal mass, m_i, is depicted in Figure 3.28. Simulation time with five masses was found to be within a reasonable range for model development.

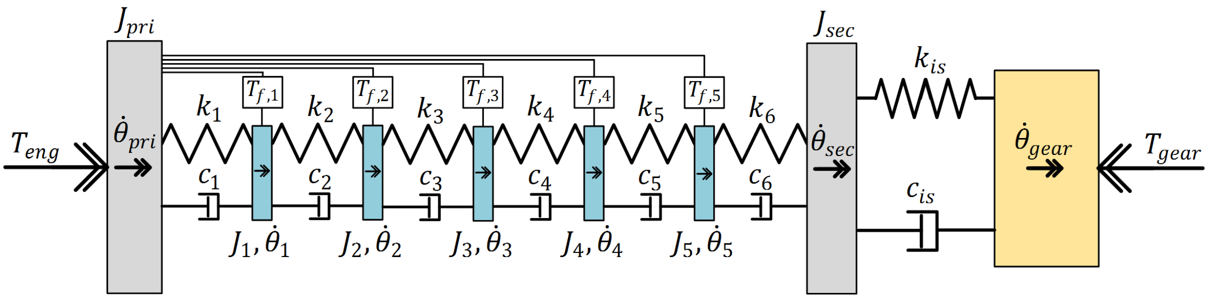

Figure 3.28: Engineering model with five DOF of the arc-spring

The physical- and geometrical parameters for the arc-spring used in the modelling are presented in Table 3.7.

Table 3.7: Arc-spring physical- and geometrical parameters

m	μ	r	D
[kg]	$[-]$	[m]	[m]
1	0.1	0.1625	0.040

The system is initially at stationary speed and zero displacement. It is loaded with the engine torque, T_{eng}, on the primary flywheel and bounded by the constant motion, $\dot{\theta}_{gear}$, on the input shaft of the gearbox. In the end the relative displacement, velocity, acceleration and transmitted torque between the flywheels can be obtained.

3.3.2 Mathematical model

Newton's second law of rotational motion applied on the engineering model in Figure 3.27, can be obtained using the FBD method. The equations for the primary flywheel, arc-spring and the secondary flywheel are expressed in the Eqs. (3.8), (3.9) and (3.10) respectively as

$$J_{pri}\ddot{\theta}_{pri} = T_{eng} - \underbrace{c_1(\dot{\theta}_{pri} - \dot{\theta}_1)}_{T_{d,1}} - \underbrace{k_1(\theta_{pri} - \theta_1)}_{T_{s,1}} - T_{f,pri} \Rightarrow$$

$$J_{pri}\ddot{\theta}_{pri} = T_{eng} - T_{d,1} - T_{s,1} - T_{f,pri} \tag{3.8}$$

$$J_i\ddot{\theta}_i = T_{d,i} - T_{d,i+1} + T_{s,i} - T_{s,i+1} + T_{f,i}\ , \quad i = 1, .., N \tag{3.9}$$

$$J_{sec}\ddot{\theta}_{sec} = \underbrace{c_{N+1}(\dot{\theta}_N - \dot{\theta}_{sec})}_{T_{d,N+1}} + \underbrace{k_{N+1}(\theta_N - \theta_{sec})}_{T_{s,N+1}} - \underbrace{k_{is}(\theta_{sec} - \theta_{gear}) - c_{is}(\dot{\theta}_{sec} - \dot{\theta}_{gear})}_{T_{is}} \Rightarrow$$

$$J_{sec}\ddot{\theta}_{sec} = T_{d,N+1} + T_{s,N+1} - T_{is} \tag{3.10}$$

Note that here the absolute angular displacement for the primary flywheel is equal to $\theta_{pri} = \theta_0$ and for the secondary flywheel $\theta_{sec} = \theta_{N+1}$. The friction torque, $T_{f,pri} = \sum_{i=1}^{N} T_{f,i}$, i.e. the sum of all the frictional torque from the spring masses. The Eqs. (3.8) and (3.10) for the primary- and the secondary flywheel are almost the same as for the linear spring system in section 3.1.2. The difference now is seen in Eq. (3.8) where the frictional torque, $T_{f,pri}$, is included.

Since the arc-spring is divided into N number of masses, the stiffness and the damping for the spring elements can be computed using Eq. (3.11) if the spring elements have the same stiffness k_i

$$\frac{1}{k_{eq}} = \left(\sum_{i}^{N} \frac{1}{k_i}\right) \Rightarrow$$

$$k_i = N k_{eq} \tag{3.11}$$

The viscous damping, c_i, can be computed in the same way as the stiffness

$$c_i = N c_{eq} \tag{3.12}$$

Modified sine engine torque

The engine torque, T_{eng}, that was used earlier in the simulations had a low mean value and amplitude compared to the realistic engine torque, see section 3.1.2. Thereby the mean value, T_0, was increased from 300 to 3000 Nm and the amplitude, T_A, from 500 to 2000 Nm, see Eq. (3.13)

$$T_{eng}(t) = T_0 + T_A sin(\omega_{3rd}t + \psi) = 3000 + 2000 sin(\omega_{3rd}t) \tag{3.13}$$

The frequency, ω_{3rd}, is the third engine order vibration, i.e. three times the angular velocity of the crankshaft, $\omega_{3rd} = 3\omega$. The angular velocity of the crankshaft was computed as $\omega = \frac{2\pi n}{60}$, where n is the engine speed in rpm.

Modelling of the frictional torque

The FBD of the arc-spring is shown in Figure 3.29.

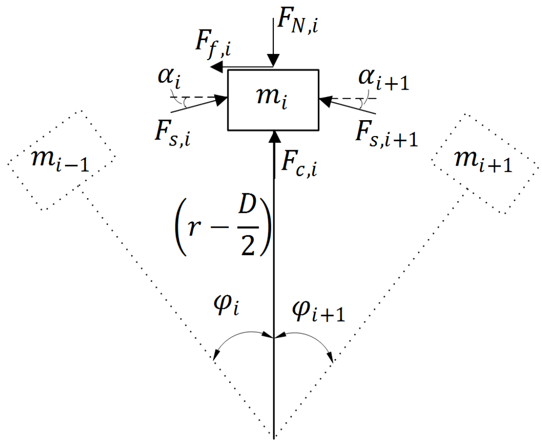

Figure 3.29: FBD of the mass elements of the arc-spring

The equilibrium equations in horizontal- and vertical direction for the mass element, m_i, of the arc-spring can be expressed as Eqs. (3.14) and (3.15)

$$\rightarrow: \; F_{s,i}cos(\alpha_i) - F_{s,i+1}cos(\alpha_{i+1}) - F_{f,i} = m_i a_s = m_i r \ddot{\theta}_i \tag{3.14}$$

$$\uparrow: \; F_{c,i} - F_{N,i} + F_{s,i}sin(\alpha_i) + F_{s,i+1}sin(\alpha_{i+1}) = 0 \tag{3.15}$$

Rewriting Eq. (3.15) the normal force, $F_{N,i}$, can be obtained as

$$F_{N,i} = F_{c,i} + F_{s,i}sin(\alpha_i) + F_{s,i+1}sin(\alpha_{i+1}) \tag{3.16}$$

The angle, α_j, can be computed as Eq. (3.17), where $\phi_{0,j}$ is the angle between two mass elements of the arc-spring at unloaded condition, $(j = 1, .., N + 1)$.

$$\alpha_j = \frac{\varphi_j}{2} = \frac{1}{2}(\Phi_{0,j} + \Delta\varphi_j) = \frac{1}{2}(\phi_{0,j} - |\theta_{j-1} - \theta_j|) \tag{3.17}$$

The arc-springs have been approximated as one in this mathematical model. This approximation removes the symmetric behaviour of the DMF. To obtain a symmetrical behaviour, in both positive and negative relative angular displacement, the relative angle $\theta_{j-1} - \theta_j$ in Eq. (3.17) has to be absolute.

The normal force, F_N, is now a function of both the centrifugal force, F_c, and the spring compression, F_s. The centrifugal force, $F_{c,i}$, can be computed using Eq. (3.18), where the radius to the arc-spring is denoted by r.

$$F_{c,i} = m_i r \dot{\theta}_i^2 \tag{3.18}$$

The force from the spring compression, $F_{s,j}$, can be computed as Eq. (3.19), (where $j = 1, .., N + 1$).

$$F_{s,j} = \frac{T_{s,j}}{r} = \frac{k_j}{r}\bigg(\theta_{j-1} - \theta_j\bigg) \tag{3.19}$$

Here $(\theta_{j-1} - \theta_j)$ will define the compression of the spring element, i.

The normal force in Eq. (3.16) can now be used for computing the frictional force using a chosen friction model as Coulomb- or LuGre friction model, etc.

The Coulomb friction model was used to model the friction response on the mass elements, m_i in this stage and the frictional torque, $T_{f,i}$, can then be computed as Eq. (3.20).

$$T_{f,i} = \mu\bigg(r + \frac{D}{2}\bigg)|F_{N,i}|sign(\dot{\theta}_{pri} - \dot{\theta}_i) \tag{3.20}$$

Here $(r + \frac{D}{2})$ is the radius to the outer edge of the arc-spring (i.e. to the channel in the primary flywheel where the friction will appear).

The mathematical model, written on matrix form, considering the linear parts and the nonlinear part due to friction from the arc-spring, is expressed as Eq. (3.21).

$$\underbrace{\underline{\boldsymbol{J}}\ddot{\boldsymbol{\theta}} + \underline{\boldsymbol{C}}\dot{\boldsymbol{\theta}} + \underline{\boldsymbol{K}}\boldsymbol{\theta}}_{\text{Linear}} + \underbrace{\underline{\boldsymbol{C}}_{NL}\dot{\boldsymbol{\theta}}}_{\text{Non-linear}} = \boldsymbol{T} \tag{3.21}$$

The non-linear part is added to the right hand side (RHS) which gives that Eq. (3.21) can be expressed as Eq. (3.22).

$$\underbrace{\underline{\boldsymbol{J}}\ddot{\boldsymbol{\theta}} + \underline{\boldsymbol{C}}\dot{\boldsymbol{\theta}} + \underline{\boldsymbol{K}}\boldsymbol{\theta}}_{\text{Linear}} = \boldsymbol{T} - \underbrace{\underline{\boldsymbol{C}}_{NL}\dot{\boldsymbol{\theta}}}_{\text{Non-linear}} \tag{3.22}$$

The non-linear part can be expressed as Eq. (3.23), where the frictional damping is equal to, $c_{f,i} = \frac{\mu(r+\frac{D}{2})|F_{N,i}|}{|\dot{\theta}_{pri}-\dot{\theta}_i|}$, which can be related to Eq. (3.20). Here the arc-spring is divided into two mass elements, m_1 and m_2.

$$\underline{\boldsymbol{C}}_{NL}\dot{\boldsymbol{\theta}} = \begin{bmatrix} c_{f,1} + c_{f,2} & -c_{f,1} & -c_{f,2} & 0 \\ -c_{f,1} & c_{f,1} & 0 & 0 \\ -c_{f,2} & 0 & c_{f,2} & 0 \\ 0 & 0 & 0 & 0 \end{bmatrix} \begin{bmatrix} \dot{\theta}_{pri} \\ \dot{\theta}_1 \\ \dot{\theta}_2 \\ \dot{\theta}_{sec} \end{bmatrix} = \begin{bmatrix} T_{f,1} + T_{f,2} \\ -T_{f,1} \\ -T_{f,2} \\ 0 \end{bmatrix} \tag{3.23}$$

Torque response of the DMF at standstill primary flywheel

The transmitted torque from the DMF at an applied angular displacement on the input shaft of the gearbox, θ_{gear}, was analysed for a standstill case of the primary flywheel, $\theta_{pri} = 0$. To model this the mathematical model was modified by changing the boundary conditions (BC's). Thereby for this case the engine torque, $T_{eng} = 0$.

To easier explain the modelling, the arc-spring is considered to have two mass elements, m_i, $i = 1, 2$. The Newton's second law for the primary flywheel Eq. (3.24), arc-spring masses Eqs. (3.25), (3.26) and the secondary flywheel Eq. (3.27) can expressed as

$$J_{pri}\ddot{\theta}_{pri} + c_1(\dot{\theta}_{pri} - \dot{\theta}_1) + k_1(\theta_{pri} - \theta_1) = -(T_{f,1} + T_{f,2}) \tag{3.24}$$

$$J_1\ddot{\theta}_1 + c_2(\dot{\theta}_1 - \dot{\theta}_2) - c_1(\dot{\theta}_{pri} - \dot{\theta}_1) + k_2(\theta_1 - \theta_2) - k_1(\theta_{pri} - \theta_1) = T_{f,1} \tag{3.25}$$

$$J_2\ddot{\theta}_2 + c_3(\dot{\theta}_2 - \dot{\theta}_{sec}) - c_2(\dot{\theta}_1 - \dot{\theta}_2) + k_3(\theta_2 - \theta_{sec}) - k_2(\theta_1 - \theta_2) = T_{f,2} \tag{3.26}$$

$$J_{sec}\ddot{\theta}_{sec} - c_3(\dot{\theta}_2 - \dot{\theta}_{sec}) + c_{is}\dot{\theta}_{sec} - k_3(\theta_2 - \theta_{sec}) + k_{is}\theta_{sec} = c_{is}\dot{\theta}_{gear} + k_{is}\theta_{gear} \tag{3.27}$$

The BC for the primary flywheel, $\theta_{pri} = 0$, gives that Eq. (3.24) and Eq. (3.25) can be reduced to the following equations

$$-c_1\dot{\theta}_1 - k_1\theta_1 = -(T_{f,1} + T_{f,2}) \tag{3.28}$$

$$J_1\ddot{\theta}_1 + c_2(\dot{\theta}_1 - \dot{\theta}_2) + c_1\dot{\theta}_1 + k_2(\theta_1 - \theta_2) + k_1\theta_1 = T_{f,1} \tag{3.29}$$

The reduced equation for the primary flywheel, Eq. (3.28), inserted into Eq. (3.29) gives

$$J_1\ddot{\theta}_1 + c_2(\dot{\theta}_1 - \dot{\theta}_2) + k_2(\theta_1 - \theta_2) = -T_{f,2} \tag{3.30}$$

The angular displacement was applied on the input shaft of the gearbox, θ_{gear}, in order to include the whole engineering model, instead of applying the angular displacement directly on the secondary flywheel. It was modelled as a sine load with an amplitude, A, and a period of one second (i.e $sin(2\pi t)$) as Eq. (3.31). The applied angular displacement varies between $\pm\Phi$, (maximum/minimum angle in degrees), as the following equation

$$\theta_{gear} = Asin(2\pi t) = \Phi\frac{\pi}{180^\circ}sin(2\pi t) \tag{3.31}$$

3.3.3 Computational model

Python

The system was solved in the same way as before using Newmark-Beta method and Newton iterations by the function fsolve in Python.

The frictional torque, $T_{f,i}$, considering Coulomb friction in Eq. (3.20) was modelled as a stepwise function due to the $sign(\dot{\theta}_{pri} - \dot{\theta}_i)$ part. To obtain a more stable solution when solving the problem, the equation was modified by using a continuous function, inverse tangent, in Figure 3.30 for the $sign$ part in Eq. (3.20).

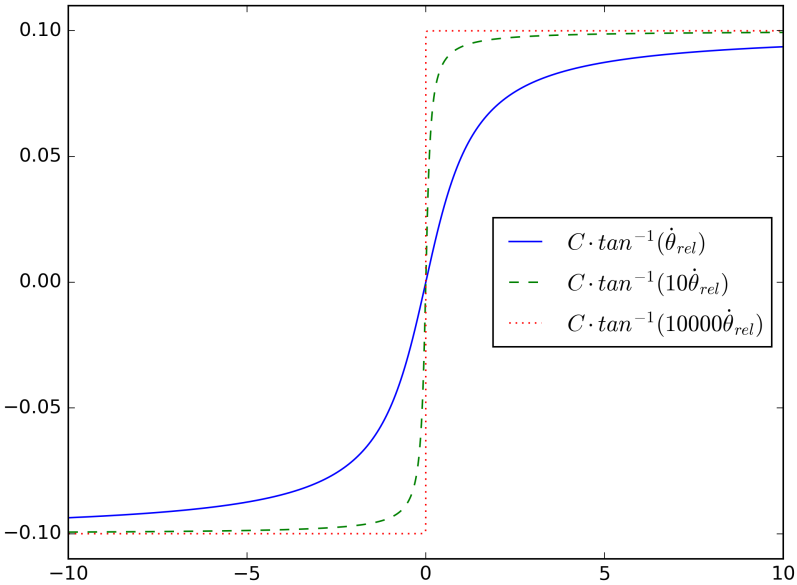

Figure 3.30: Arcus tangens function for modelling the Coulomb friction with constant normal force $F_N = 1$

In the code the function $C(t) \cdot tan^{-1}(10\dot{\theta}_{rel})$ was used which gives that Eq. (3.20) can be rewritten as

$$T_{f,i} = \underbrace{\frac{\mu(r + \frac{D}{2})|F_{N,i}|}{\frac{\pi}{2}}}_{C(t)} tan^{-1}\Big(10(\dot{\theta}_{pri} - \dot{\theta}_i)\Big) \tag{3.32}$$

Note that the factor $C(t)$ is a function of time, that is because the normal force can change in time due to angular velocity and spring compression. The relative angular velocity between the primary flywheel and the arc-spring masses, $\dot{\theta}_{pri} - \dot{\theta}_i$, was denoted as $\dot{\theta}_{rel}$ in Figure 3.30.

AVL

The serial springs and dampers in Spring1 - Spring6 were implemented according to Eq. (3.11). The frictional contributions are defined as moments calculated from the normal forces in F_1 to F_6 and applied in the opposite direction of the relative angular velocity. The inverse tangent approximation, Eq. (3.32), of the Coulomb friction model was used. To get the result of the primary wheel in relation to the secondary a connection (rel_vel) with zero stiffness was added between the two wheels. All parameters that were needed for this model are summarized in Appendix A.3. Detailed description of the model elements can be found in Appendix B.

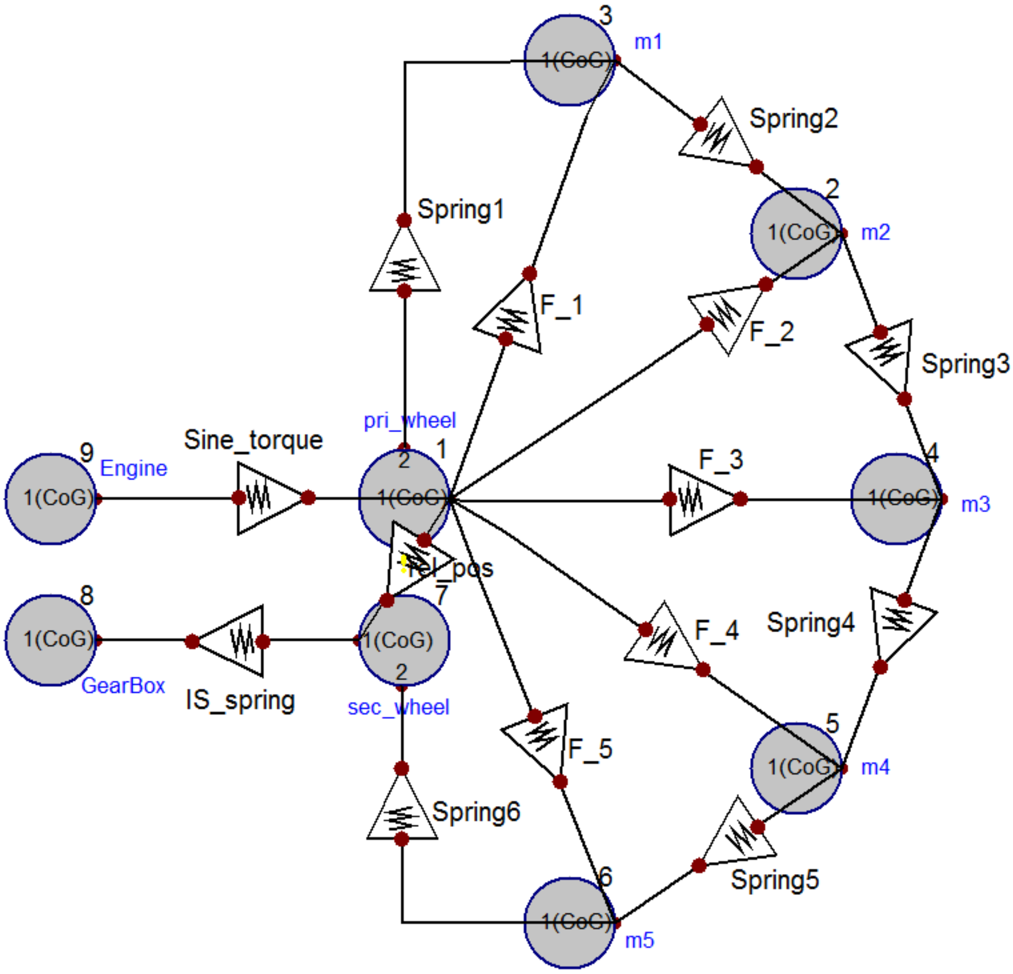

Figure 3.31: Graphical model AVL, 5 spring model

The compression of the translational spring will be less than if the compression follows the arc of the spring, see Figure 3.32. The definition of the translational stiffness is according to Eq. (3.33).

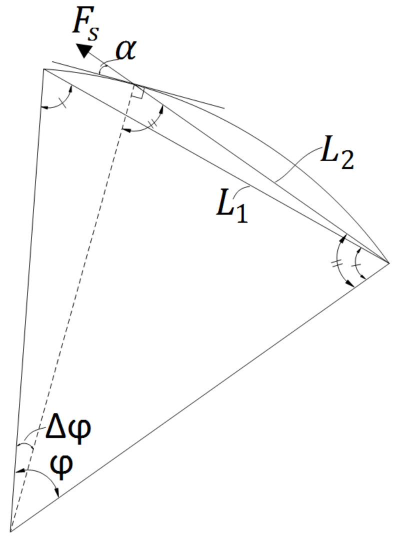

Figure 3.32: Schematic of the angles for engineering model of translational springs

$$T_\varphi = k_\varphi \Delta\varphi$$

$$T_s = k_s(L_1 - L_2)r \cdot cos(\frac{\varphi}{2} - \frac{\Delta\varphi}{2})$$

where

$$L_1 = 2r \cdot sin(\frac{\varphi}{2})$$

$$L_2 = 2r \cdot sin(\frac{\varphi - \Delta\varphi}{2})$$

Equality between the torque given by the rotational and the translational spring is sought, $T_\varphi = T_s$. Under the assumption of small oscillations $\Delta\varphi$, the following equation is obtained

$$k_s = k_\varphi \frac{1}{r_{spring}^2 \cdot cos^2(\frac{\varphi}{2})} \tag{3.33}$$

φ is the angle a mass should oscillate around with a given mean load and given number of spring masses.

3.3.4 Result

The eigenvalues for this friction model (Model 3) were calculated using Eq. (2.12) in the same way as for the other models. The natural undamped eigenfrequencies are presented in Table 3.8. Even for this system the second eigenfrequency is located around the engine speed of 800 rpm for the both sets of material parameters. High torsional vibrations ($\theta_{pri} - \theta_{sec}$) of the system are thereby expected to appear at the engine speed of 800 rpm.

Table 3.8: The four first undamped eigenfrequencies for the friction model				
Eigenmode	1	2	3	4
Structural parameters A, $\frac{\omega_n}{3}$ [rpm]	303.97	1421.44	7908.53	15195.44
Structural parameters B, $\frac{\omega_n}{3}$ [rpm]	349.43	818.82	6298.97	12119.61
Structural parameters A, ω_{3rd} [Hz]	15.20	71.07	395.43	759.77
Structural parameters B, ω_{3rd} [Hz]	17.47	40.94	314.95	605.98

The friction model for the Python model was initially evaluated against the linear spring model presented in section 3.1. For this evaluation, the structural parameters B were used in Table 3.1. The physical- and geometrical parameters in Table 3.7 were used, but the mass was changed to $m = 0.001$ kg and the friction coefficient was changed to $\mu = 0$. The results are presented in the Figures 3.33 and 3.34. According to the figures it is concluded that the two different models show approximately the same result.

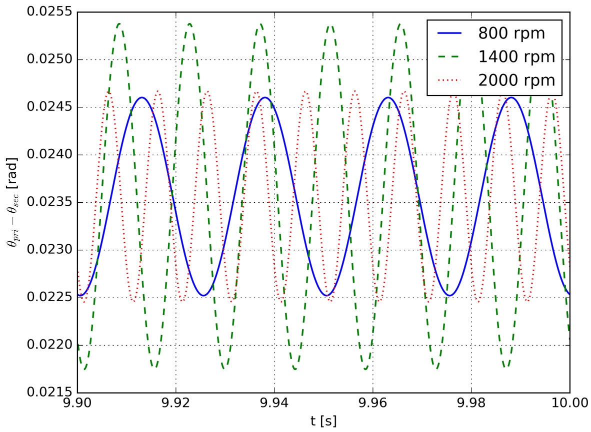

Figure 3.33: Model 3, Friction model, $\mu = 0$, Python

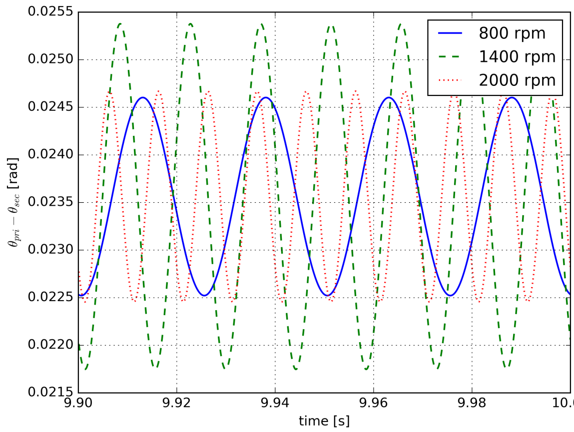

Figure 3.34: Linear spring system, Python

The torsional vibrations ($\theta_{pri} - \theta_{sec}$) have been studied for the Python- and AVL friction model, using the parameters for the arc-spring presented in Table 3.7 without any friction. The arc-spring diameter D in the Python model was neglected, due to that it was not included in the AVL model. The solutions for the Python- and AVL models are presented in Figure 3.35 and 3.36 respectively. The engine load used was the sine load in Eq. (3.13) and the structural parameters C in Table 3.1. Here the equivalent damping for the arc-spring was decreased to $c_{eq} = 5$ Nms/rad compared to structural parameters B, in order not to damp the vibrations too much which could hide differences in friction modelling between the models.

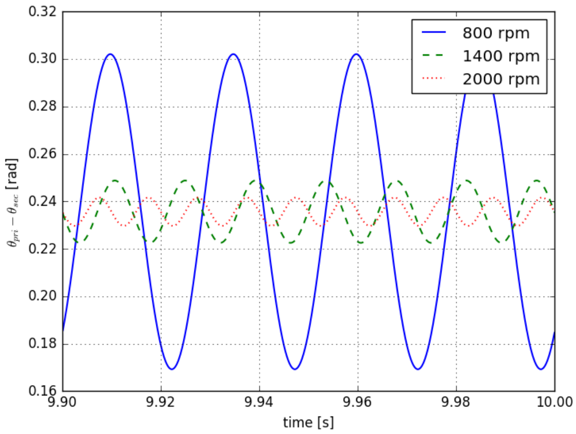

Figure 3.35: Model 3, Friction model, $\mu = 0$, Python

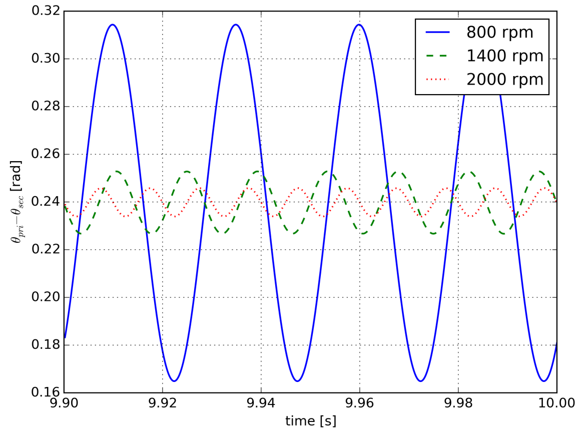

Figure 3.36: Model 3, Friction model, $\mu = 0$, AVL

The RMS values for the results for the different models in Figure 3.35 and 3.36 are gathered in Table 3.9.

Table 3.9: RMS values for the friction model without friction, $\mu = 0$

Engine speed [rpm]	800		1400		2000	
Software	Python	AVL	Python	AVL	Python	AVL
RMS	0.24032621	0.24523061	0.23581179	0.23970253	0.23566672	0.23966317

The models in Figures 3.35 and 3.36 compare well to each other. The deviations in the models, regarding RMS value, can be explained with the difference in the engineering model. Even though the stiffness is compensated for the reformulation of the translational stiffness, Eq. (3.33), the stiffness is only correct for the angle φ. This implies that for lower deformations than φ the stiffness is too low and for higher deformations the stiffness is too high.

Friction implemented comparison Python and AVL

When implementing the friction to the arc-spring the friction coefficient, $\mu = 0.1$ was used as in Table 3.7, in combination with the sine load computed using Eq. (3.13) and the structural parameters C in Table 3.1. The result for the relative angular displacement between the primary and secondary flywheel, $(\theta_{pri} - \theta_{sec})$, are presented in Figure 3.37 for the Python solution. The representative solution in AVL is presented in Figure 3.38.

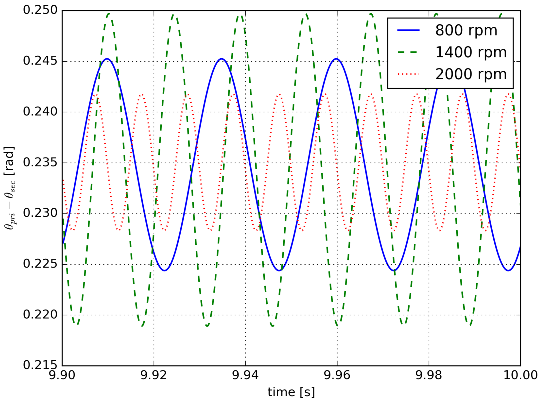

Figure 3.37: Model 3, Friction model, angular displacement, Python

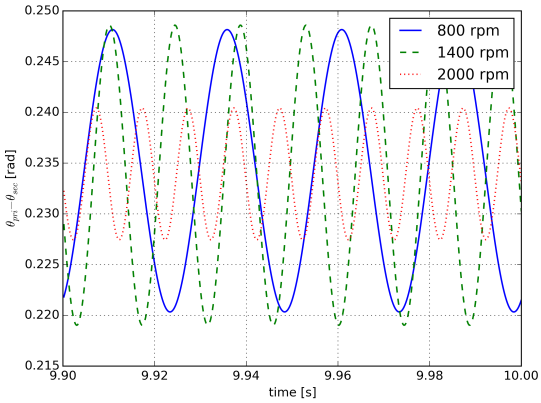

Figure 3.38: Model 3, Friction model, angular displacement, AVL

Analysis of the solutions in the Figures 3.37 and 3.38 shows that the DMF torsional vibration dynamics for the engine speed of 800 rpm has significant differences. The differences are explained with Figure 3.39. The behaviour of the frequency response is the same in both models, the small difference between the models and the high gradient at 800 rpm explains the difference.

The RMS values for each curve are gathered in Table 3.10, which shows the difference of the solution between the computational models. The stiffness is converted to translational stiffness that is correct for a specific angle, φ, using Eq. (3.33). This means that the translational spring has a small underestimation of the stiffness when winding up to φ, hence the error in RMS values in Table 3.10.

Table 3.10: RMS values for the friction models, structural parameters C

Engine speed [rpm]	800		1400		2000	
Software	Python	AVL	Python	AVL	Python	AVL
RMS	0.23489929	0.23874171	0.23454560	0.2383362	0.23510322	0.23826931

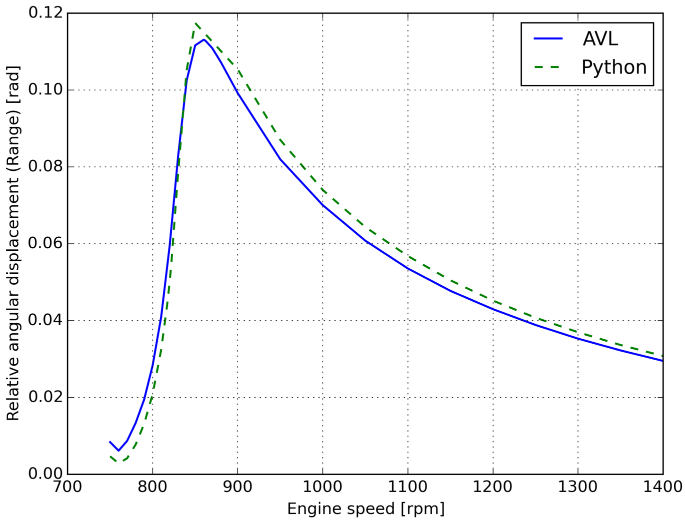

Figure 3.39: Frequency response in AVL and Python, $(\theta_{pri} - \theta_{sec})$

The solution for the torsional vibrations for the engine speeds 850, 900 and 950 rpm are presented in Figures 3.40 and 3.41. It shows that solutions between the models correlate better for these engine speeds, since the engine speeds are higher than for the second eigenmode at around 820 rpm (see Table 3.8).

The difference of the solutions between the computational models in Python and AVL have been studied. The RMS values for the solutions are presented in Table 3.11 and shows the difference between the models.

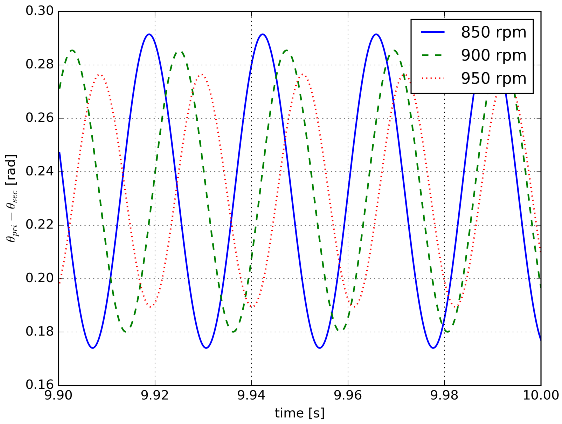

Figure 3.40: Model 3, Friction model, angular displacement, Python

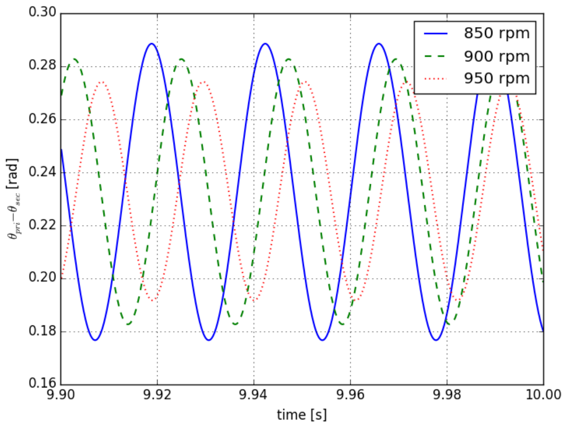

Figure 3.41: Model 3, Friction model, angular displacement, AVL

Table 3.11: RMS values for the friction models for compensated speeds

Engine speed [rpm]	850		900		950	
Software	Python	AVL	Python	AVL	Python	AVL
RMS	0.23469932	0.23855105	0.23817327	0.24175261	0.23675492	0.24064632

The systems relative angular displacement ($\theta_{pri} - \theta_{sec}$) for the Python- and AVL models have been compared and evaluated using the two computational models. The different structural parameters and engine torques were used in the computational model in the same way as for model 1 and model 2. The conclusion that can be drawn is that the difference in engineering model that have been introduced in this model is well compensated for. The two models have the same behaviour, see Figure 3.39, but a small deviation in the result. This small deviation is accepted and in the final results the Python model has been used.

4 Results

In the mathematical model presented in section 3.3.2 the frictional torque was modelled using the inverse tangent approximation, Eq. (3.32), of the Coulomb friction model. To make convergence easier a continuous function instead of the sign of the relative velocity between the primary flywheel and the arc-spring masses was used. The direction of the friction force/torque will then change direction due to the relative velocity. The functions $C(t) \cdot tan^{-1}(10\dot{\theta}_{rel})$ and $C(t) \cdot tan^{-1}(10000\dot{\theta}_{rel})$ were analysed in order to find the continuous function in Figure 3.30 that will give sufficiently good results. The results for the torsional vibrations are presented in the Figures 4.1 and 4.2.

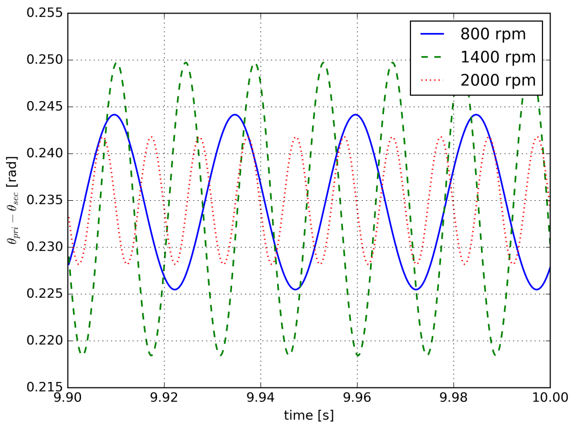

Figure 4.1: Model 3, Friction model, Coulomb friction, $C \cdot tan^{-1}(10\dot{\theta}_{rel})$

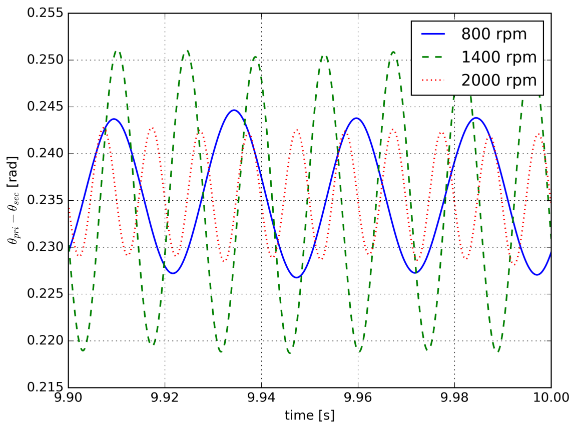

Figure 4.2: Model 3, Friction model, Coulomb friction, $C \cdot tan^{-1}(10000\dot{\theta}_{rel})$

The solution using the continuous function $C(t) \cdot tan^{-1}(10\dot{\theta}_{rel})$ shows a stable solution and sufficiently good results compared to the continuous function in Figure 4.2 which is slightly unstable but the differences in amplitude of the angular displacement are still approximately the same. Simulation time increases drastically as the argument for the inverse tangent rises but the relative angular displacement remains almost the same. Thereby the continuous function $C(t) \cdot tan^{-1}(10\dot{\theta}_{rel})$ is shown in this results to give a sufficient representation of the Coulomb friction model [11].

The engine torques for the three engine speeds transferred to the secondary flywheel are presented in Figure 4.3. These results can be compared to the applied moment from the engine, see Eq. (3.13), and the moment amplitude has been reduced according to Table 4.1.

Table 4.1: DMF moment amplitude reduction

Engine speed [rpm]	800	1400	2000
Applied load amp. [Nm]	2000	2000	2000
Simulated response amp. [Nm]	303.02	317.25	213.42
Reduction [%]	84.85	84.14	89.33

The normal forces considering centripetal force and spring compression that are acting on the five masses of the arc-spring have been studied for an operating speed range of 800 to 6000 rpm. This shows which component that will have the highest contribution to the normal force at different engine speeds. The results are presented in Figure 4.4.

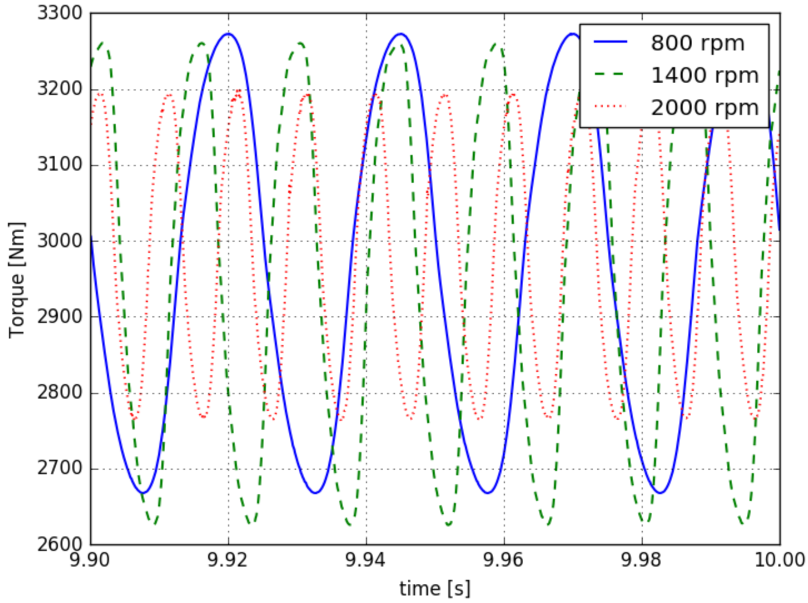

Figure 4.3: Model 3, Torque secondary flywheel, Python

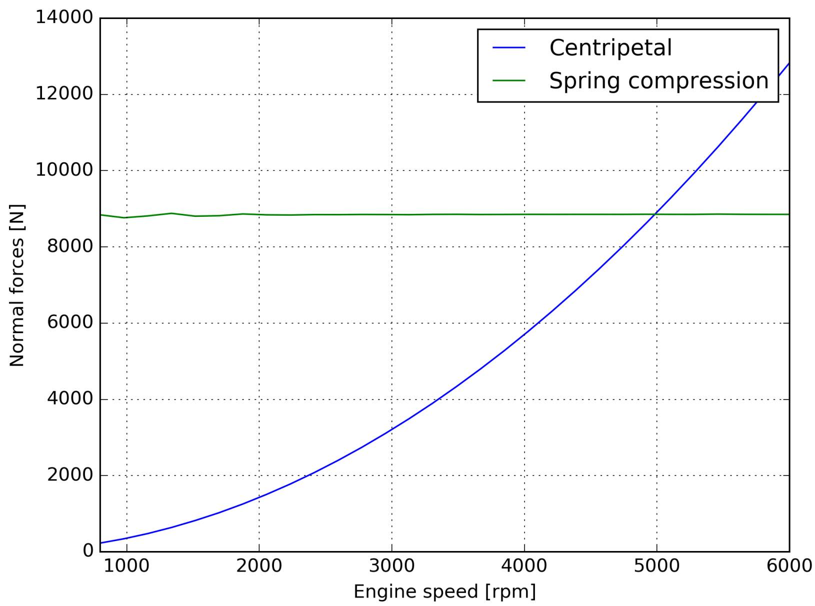

Figure 4.4: Normal forces from centripetal and spring compression

The studied operating speed range was chosen to be large, in order to be able to analyse the difference between DMF for trucks and cars, since cars have higher operating speeds.

The frictional torque that was computed using Eq. (3.32) for the five masses on the arc-spring are presented in Figure 4.5.

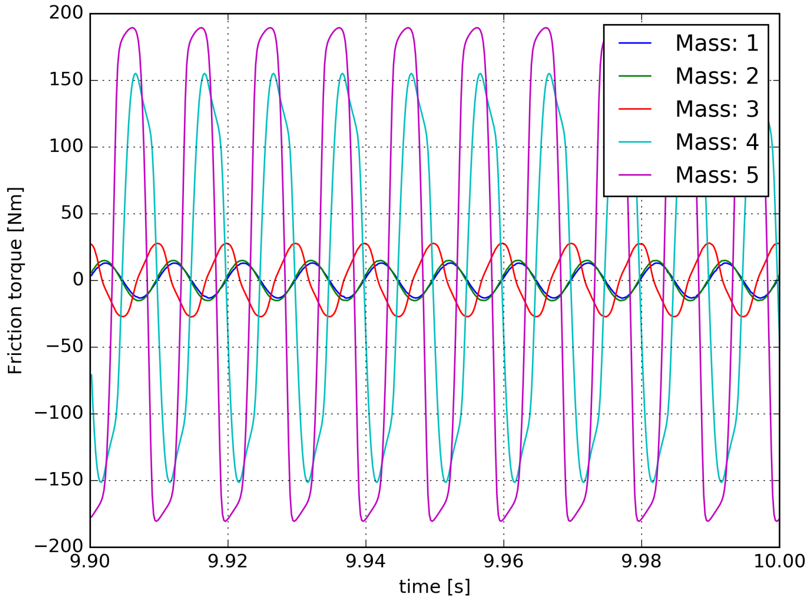

Figure 4.5: Model 3, Friction model, friction torque for all the masses

The results show that there are higher amplitudes on the frictional torque for the masses that are physically located longer from the primary flywheel. This is due to that the relative velocities are larger for those masses. This can also be analysed in Eq. (3.32) using the continuous function. The results are thereby reasonable.

A simulation where the number of spring masses are changed has been performed. The simulation contains result from one single mass up to 30 masses. The sum of all friction moments for a given time was calculated. This have been done for all timesteps and used to calculate the RMS value of the frictional torque, T_f, for all sets of masses. The result is presented in Figure 4.6. It should be noted that for five masses the friction has not converged. There is a trade-off for simulation time and accuracy when choosing number of masses. With Figure 4.6 the accuracy can still be conserved with few masses if the friction model is adjusted accordingly. Convergence is obtained in the whole speed range for a truck engine. If the result with 30 masses is assumed to be the exact solution, then the result from five masses needs to be calculated with a friction coefficient of $C_{ext}(n)\mu$, assuming that the friction moment can be linearly extrapolated. This parameter changes with engine speed according to Table 4.2.

Table 4.2: Linear extrapolation parameters for μ

Engine speed [rpm]	800	1400	2000
$C_{ext}(n)$	0.92878	1.09376	1.18159

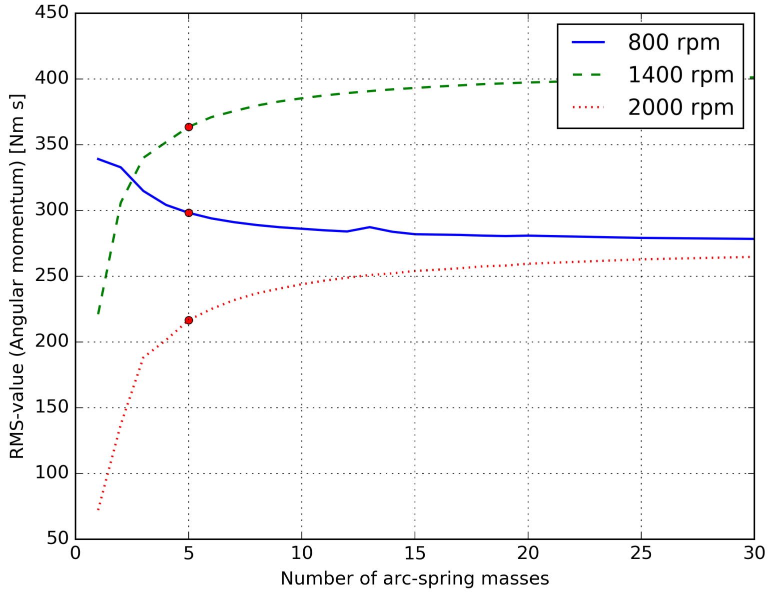

Figure 4.6: Model 3, Friction model, convergence plot of the arc-spring masses

The simulation times of the DMF torsional vibration dynamics have been studied for different number of arc-spring masses, for the three different engine speeds. The results are presented in Figure 4.7.

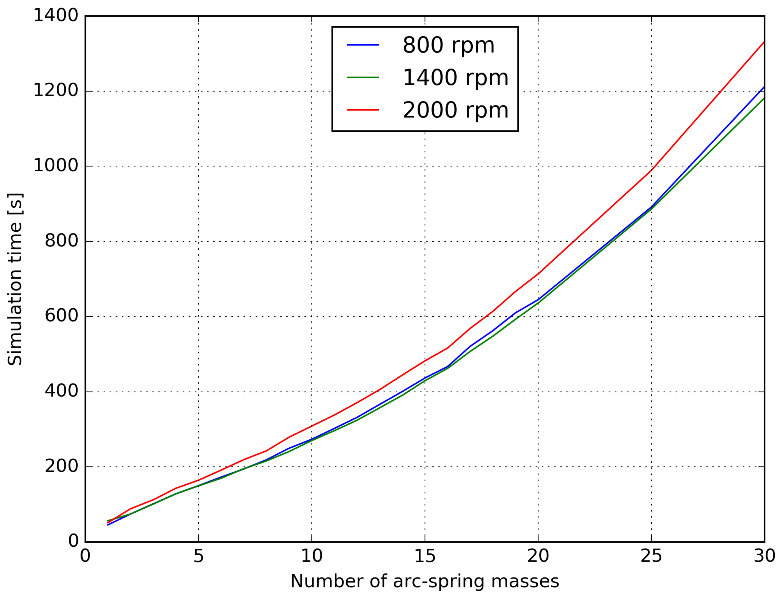

Figure 4.7: Model 3, Friction model, simulation time for different number of arc-spring masses

The simulation times for all the three different engine speeds shows the same exponential behaviour. For five number of arc-spring masses the simulation times are approximately the same. With a larger number of arc-spring masses the simulation times differs more for the different engine speeds. Simulation time is increased with a factor of 8.03 (mean of the three speeds) for 30 masses compared to five masses.

Transmitted torque response of the DMF

The transmitted torque from the DMF at standstill case of the primary flywheel ($\theta_{pri} = 0$) was studied. The response was computed using the structural parameters C in Table 3.1, for the angular displacement, θ_{gear}, varying between $\pm 10°$, presented in Figure 4.8.

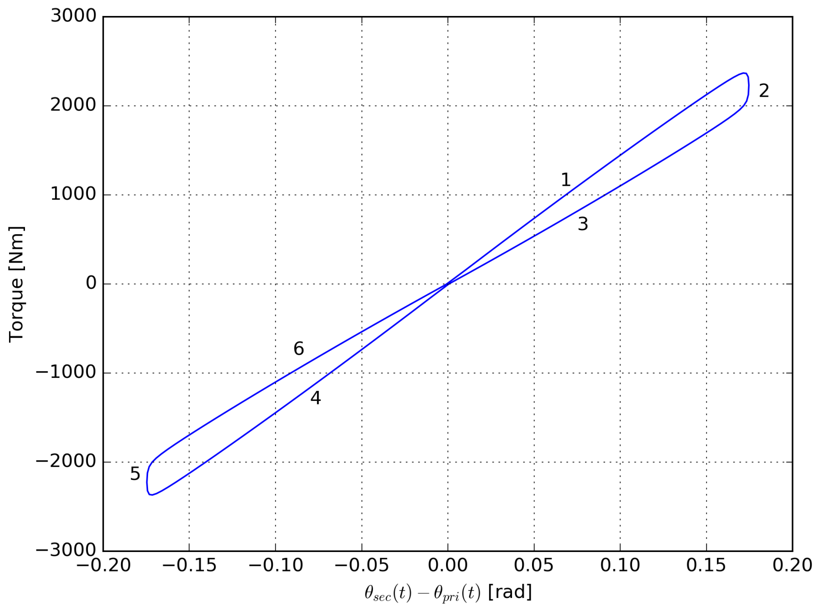

Figure 4.8: Transmitted torque from the DMF at standstill of the primary flywheel

The transmitted torque is presented as a function of the difference in angular displacement between the secondary and the primary flywheel. As can be seen the angle varies between a lower value than ± 0.175 rad ($\pm 10°$), since there is a stiffness between the input shaft of the gearbox and the secondary flywheel. Note that the response in the third quadrant of Figure 4.8 is still dissipating energy, part 4 of the Torque is the first part of the negative load.

5 Conclusions and Outlook

Two different computational models have been developed, one using Python and one using AVL. Both models include the friction behaviour created by the contact between the primary flywheel and the arc-spring.

From sections 3.1.4, 3.2.4 and the conclusion about model results being accurate can be drawn. The models are accurate according to each other and can be modified to fit experimental data. The dynamics of the DMF can be seen to be affected by the resonance at speeds close to 800 rpm if the damping and friction coefficients are very low. Relative displacement around resonance speed, with realistic friction coefficient and viscous damping, have tolerable amplitudes.

The friction is dominated by the contribution from the spring compression in the usual speed range for a truck engine. At 2000 rpm the centrifugal force contributing to the friction is approximately 13.9 %. This is not the case for a car engine with a significantly higher engine speed. At 5000 rpm the centrifugal force and spring compression contributes the same amount to the friction moment. This conclusion is drawn from current structural and physical parameters. Depending on if the DMF has full arc-springs or if the spring is designed with several linear springs connected in series, model 3 in Python or AVL will correlate better. With linear springs compressed with a rotating motion the response is not completely linear, hence translational springs and DOF should be used to capture this response. It can be concluded, for small oscillations and using linear springs in series, that the response is similar to the arc-spring. With the spring divided into N linear springs the response would also be equal to the arc-spring as $N \to \infty$.

The Coulomb friction model can be approximated with an inverse tangent function, with the argument ten times the relative angular velocity $\dot{\theta}_{pri} - \dot{\theta}_i$. This significantly reduces simulation time and still keeps good accuracy in the result. It can not be concluded that this is a perfect representation of the reality. To conclude an accurate friction model experiments need to be done. For vibration evaluation, a perfect match of friction model is not always important. In the future an equivalent damping coefficient should be investigated. It can be concluded that this equivalent damping need to be a function of engine speed, see Figure 4.6.

A convergence study was performed of the number of arc-spring masses that will be needed to obtain sufficiently good result of the frictional torques, T_f. This was presented in Figure 4.6 and it is concluded that for five arc-spring masses the computed RMS values of the torques, T_f, have not converged. This result can still be used to compensate the frictional coefficient, μ, with the extrapolated values in Table 4.2 and thereby reduce the simulation time and still achieve high accuracy.

As future work the following is suggested

- Include standstill criterion in the friction model for the arc-spring masses
- Extend model 3, mathematical model, for the standstill case to dynamical one
- Validate the dynamical model against experimental data, adjust the structural parameters accordingly
- Implement the DMF model in a model of the full truck

References

[1] *Volvo trucks image and film gallery.* 2017. URL: http://images.volvotrucks.com/ (visited on 05/24/2017).

[2] A. Nieman. *The right solution for downsped engines.* 2014. URL: http://www.danacv.com/advantek40/pdf/downspeeding_whitepaper.pdf (visited on 04/25/2017).

[3] H. Faust. *Powertrain Systems of the Future.* 2014. URL: http://www.schaeffler.com/remotemedien/media/_shared_media/08_media_library/01_publications/schaeffler_2/symposia_1/downloads_11/schaeffler_kolloquium_2014_02_en.pdf (visited on 04/25/2017).

[4] P. Kelly, B. Pennec, R. Seebacher, et al. "Dual mass flywheel as a means of attenuating rattle". *Tribology and Dynamics of Engine and Powertrain.* 1st ed. Woodhead Publishing Limited, 2010, pp. 857–877. ISBN: 978-1-845-69993-2.

[5] *Dual-mass flywheel.* 2017. URL: http://www.my-cardictionary.com/drive-train/dual-mass-flywheel.html (visited on 05/23/2017).

[6] *Volvo Trucks FH-series driveline specifications.* 2016. URL: http://www.volvotrucks.se/sv-se/trucks/volvo-fh-series/specifications/driveline.html (visited on 02/12/2017).

[7] *Volvo Cars V90 driveline specifications.* 2017. URL: http://www.volvocars.com/se/bilar/modeller/v90-cross-country/specifikationer (visited on 02/12/2017).

[8] L. Quan Songa, L. Ping Zenga, S. Ping Zhanga, et al. Design and analysis of a dual mass flywheel with continuously variable stiffness based on compensation principle. *Mechanism and Machine Theory* **79** (2014), 124–140. DOI: 10.1016/j.mechmachtheory.2014.04.004.

[9] U. Schaper, O. Sawodny, T. Mahl, et al. Modeling and torque estimation of an automotive Dual Mass Flywheel. *American Control Conference* (2009), 517–523. DOI: 10.1109/ACC.2009.5160136.

[10] T. Mahl and O. Sawodny. Modelling of an automotive dual mass flywheel. *IFAC Proceeding Volumes* **43**.18 (2010), 517–523. DOI: 10.3182/20100913-3-US-2015.00069.

[11] P. Korondi, J. Halas, K. Samu, et al. *Robot Applications.* 2014. URL: http://www.mogi.bme.hu/TAMOP/robot_applications/ch07.html (visited on 03/27/2017).

[12] R. R. Craig. and A. J. Kurdila. *Fundamentals of Structural Dynamics 2nd Edition.* John Wiley Sons inc., 2006. ISBN: 978-0-471-43044-5.

[13] J. C. Meza. Newton's method. *Wiley interdisciplinary reviews. Computational statistics* **3**.1 (2010), 75–78. DOI: 10.1002/wics.129.

[14] K. Karlsson and D. Johansson. *Simulation Models of Dual Mass Flywheels - Extra Materials.* 2017. URL: https://github.com/johansd/MasterThesis_DMF (visited on 05/25/2017).

[15] G. Bourgois. *Dual Mass Flywheel for Torsional Vibrations Damping.* 2016. M.sc. Thesis, Dep. Applied Mechanics, Chalmers. URL: http://publications.lib.chalmers.se/records/fulltext/238131/238131.pdf (visited on 03/30/2017).

[16] *Python.* 2017. URL: http://www.python.org (visited on 05/21/2017).

[17] *AVL Excite.* 2017. URL: https://www.avl.com/excite (visited on 05/21/2017).

A AVL parameters

A.1 Model 1

Parameter	Type	Value	Unit
2_cycles	global	= 60*2/speed	
DATA_PATH	global	d:\AVL_data\800	
J_pri	global	1.8	kg.m^2 (Moment of Inertia)
J_sec	global	0.6	kg.m^2 (Moment of Inertia)
bool_real_load	global	0	
bool_sin_load	global	1	
c1	global	300	N.m.s/rad (Rotational Damping)
c2	global	10	N.m.s/rad (Rotational Damping)
cycle_time	global	= 60/(3*speed)	
k1	global	20000	N.m/rad (Torsional Stiffness)
k2	global	11000	N.m/rad (Torsional Stiffness)
speed	global	800	rpm (Angular Velocity)

Figure A.1: Full parameter list - model 1

A.2 Model 2

Parameter	Type	Value	Unit
2_spring_bool	global	0	
DATA_PATH	global	d:\AVL_data\800	
J1	global	1.8	kg.m^2 (Moment of Inertia)
J2	global	0.6	kg.m^2 (Moment of Inertia)
T_real	global	60*2/speed	
angle_2_2spring	global	= angle_k1	rad (Angle)
angle_k1	global	= 0.75*pi/180	
angle_k1_2	global	= angle_k1*1.000001	
c1	global	300	N.m.s/rad (Rotational Damping)
c2	global	10	N.m.s/rad (Rotational Damping)
k1	global	20000	N.m/rad (Torsional Stiffness)
k1_a_two_spring	global	=k1*2_spring_bool	N.m/rad (Torsional Stiffness)
k1_b_two_spring	global	= k1*2_spring_bool	N.m/rad (Torsional Stiffness)
k1_nodim	global	= k1 * ms_bool	
k2	global	11000	N.m/rad (Torsional Stiffness)
load_cycle	global	= 60/(speed_rpm*3)	
ms_bool	global	1	
pi	global	= 4*atan(1)	
real_bool	global	1	
sine_bool	global	1	
speed_rpm	global	800	rpm (Angular Velocity)

Figure A.2: Full parameter list - model 2

A.3 Model 3

Parameter	Type	Value	Unit	Parameter	Type	Value	Unit
T_load	global	= 60/(3*speed)		vy2	global	=lin_vel*cos(pi/6)	m/s (Velocity)
c1_6	global	=1.051200654*6*5/r_spring/	N.s/m (Linear Damping)	vy3	global	=lin_vel*cos(0)	m/s (Velocity)
c2	global	10	N.m.s/rad (Rotational Damping)	vy4	global	=lin_vel*cos(-pi/6)	m/s (Velocity)
diff	global	=3000/k_eq/6*0		vy5	global	=lin_vel*cos(-pi/3)	m/s (Velocity)
highstiffness	global	99999999	N/m (Linear Stiffness)	x1	global	= r_spring*cos(pi/3)	m (Length)
k1_6	global	= 1.051200654*6*k_eq/r_sp	N/m (Linear Stiffness)	x2	global	= r_spring*cos(pi/6)	m (Length)
k2	global	100000	N.m/rad (Torsional Stiffness)	x3	global	= r_spring*cos(0)	m (Length)
k_eq	global	12732		x4	global	= r_spring*cos(-pi/6)	m (Length)
k_inf	global	999999999	N/m (Linear Stiffness)	x5	global	= r_spring*cos(-pi/3)	m (Length)
lin_vel	global	=speed/(60)*2*pi*r_spring	m/s (Velocity)	xf1	global	= r_spring*cos(pi/3+diff)	m (Length)
m_spring	global	= 1/5	kg (Mass)	xf2	global	= r_spring*cos(pi/6+2*diff)	m (Length)
my	global	0.1		xf3	global	= r_spring*cos(0+3*diff)	m (Length)
my_2	global	0		xf4	global	= r_spring*cos(-pi/6+4*diff)	m (Length)
pi	global	= 4*atan(1)		xf5	global	= r_spring*cos(-pi/3+5*diff)	m (Length)
r_spring	global	0.1625	m (Length)	y1	global	=r_spring*sin(pi/3)	m (Length)
r_spring_gap	global	0	m (Length)	y2	global	= r_spring*sin(pi/6)	m (Length)
r_spring_n	global	=-r_spring	m (Length)	y3	global	= r_spring*sin(0)	m (Length)
speed	global	2000	rpm (Angular Velocity)	y4	global	= r_spring*sin(-pi/6)	m (Length)
vx1	global	=-lin_vel*sin(pi/3)	m/s (Velocity)	y5	global	= r_spring*sin(-pi/3)	m (Length)
vx2	global	=-lin_vel*sin(pi/6)	m/s (Velocity)	yf1	global	=r_spring*sin(pi/3+diff)	m (Length)
vx3	global	=-lin_vel*sin(0)	m/s (Velocity)	yf2	global	= r_spring*sin(pi/6+2*diff)	m (Length)
vx4	global	=-lin_vel*sin(-pi/6)	m/s (Velocity)	yf3	global	= r_spring*sin(0+3*diff)	m (Length)
vx5	global	=-lin_vel*sin(-pi/3)	m/s (Velocity)	yf4	global	= r_spring*sin(-pi/6+4*diff)	m (Length)
vy1	global	=lin_vel*cos(pi/3)	m/s (Velocity)	yf5	global	= r_spring*sin(-pi/3+5*diff)	m (Length)

Figure A.3: Full parameter list - model 3

B Model 3 - Element setup

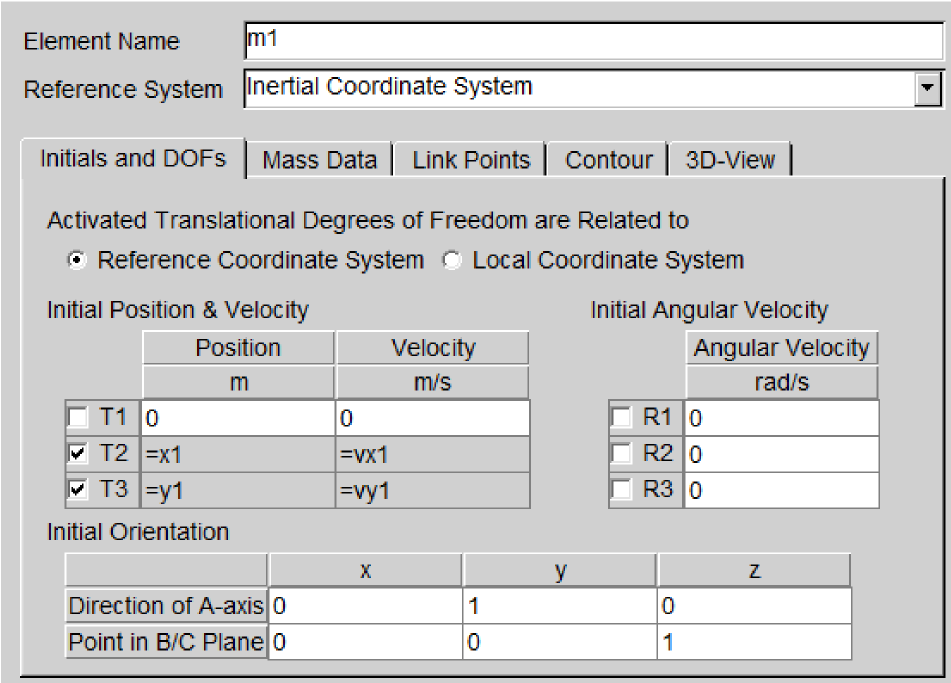

Figure B.1: Spring mass 1 - Initial conditions and DOF

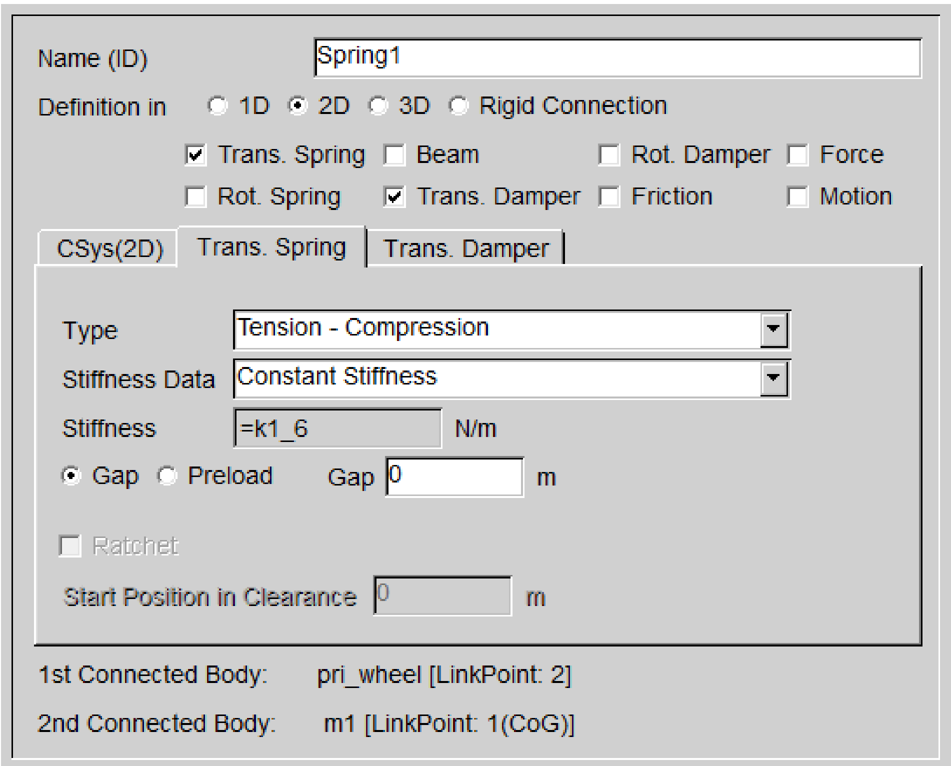

Figure B.2: Translation spring - Characteristics

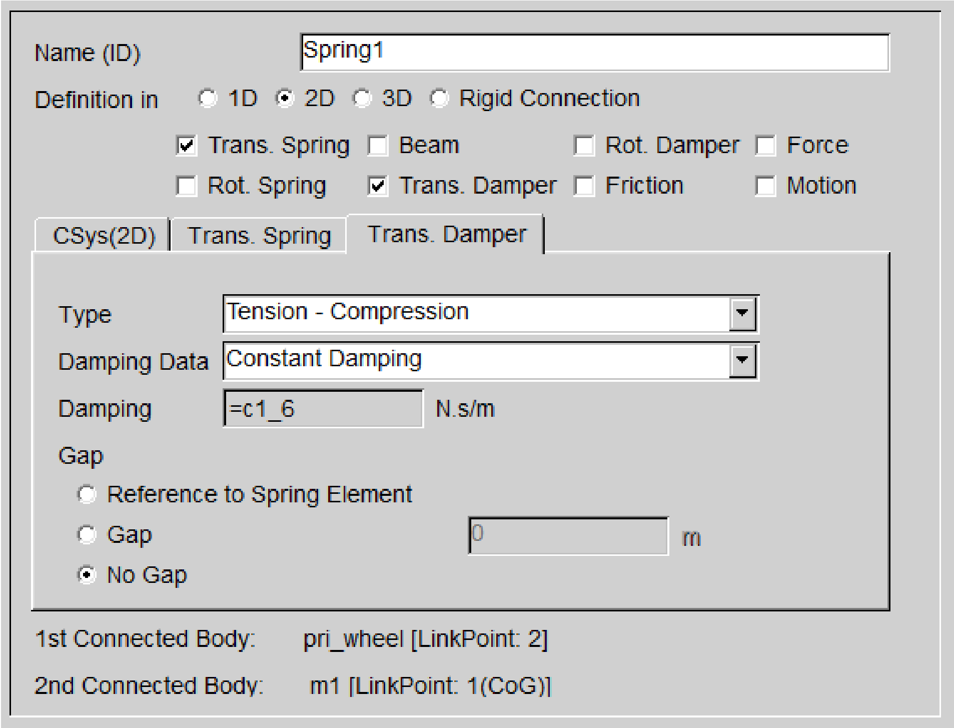

Figure B.3: Translation damper - Characteristics

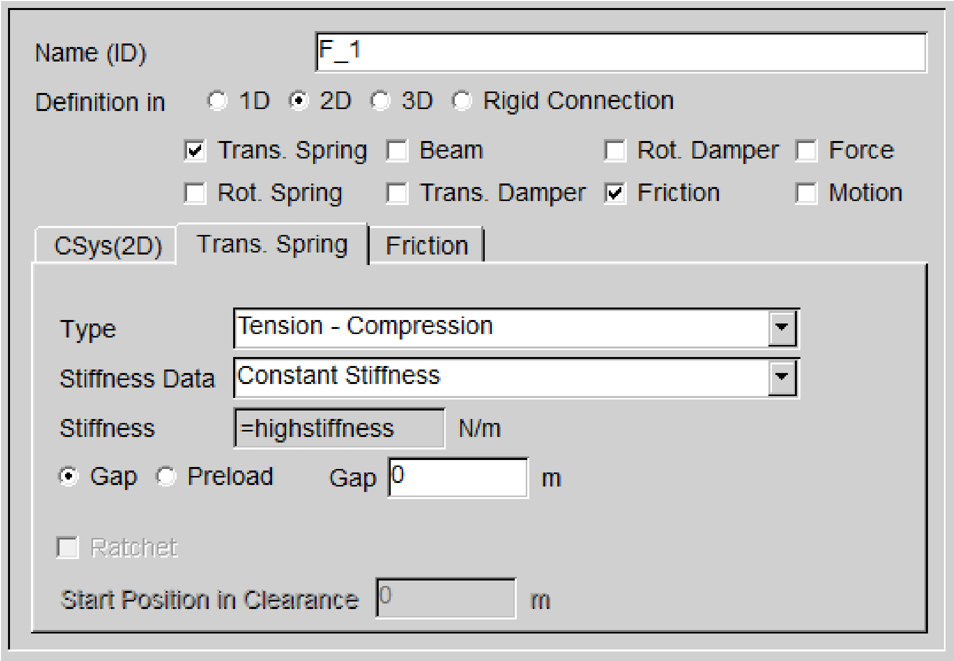

Figure B.4: Normal spring - Spring characteristics

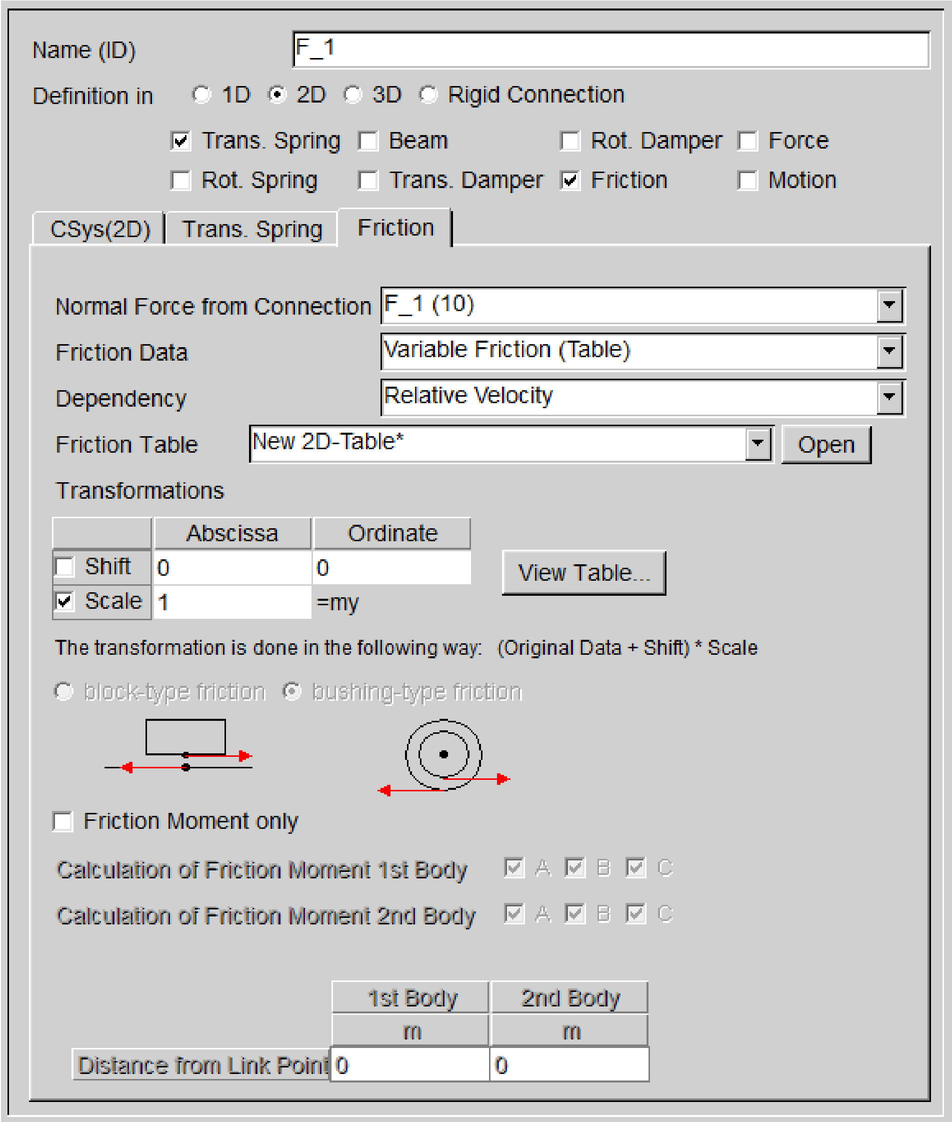

Figure B.5: Normal spring - Friction characteristics

For this model, the A-axis defines the rotary axis. This means that B- and C-axis defines the DOF of the spring masses. The springs, see Figures B.2 and B.3, is defined in the B- C-plane by a connection vector. This allows the springs to change direction as the masses moves. The direction of the normal springs, Figures B.4 and B.5, are defined with a contour plane. The spring masses are points connected to the radius of the primary wheel.